Guest-Induced Pore Breathing Controls Spin State in a Cyanido-Bridged Framework

Michał Magott*,[ab‡] Klaudia Płonka,[a‡] Barbara Sieklucka,[a] Katarzyna Dziedzic-Kocurek,[c] Wataru Kosaka,[b] Hitoshi Miyasaka*,[b] Dawid Pinkowicz*,[a]

[a] Faculty of Chemistry, Jagiellonian University, Gronostajowa 2, 30-387 Kraków, Poland

[b] Institute for Materials Research, Tohoku University, 2-1-1 Katahira, Aoba-ku, Sendai 980-8577, Japan

[c] Marian Smoluchowski Institute of Physics, Jagiellonian University, Stanisława Łojasiewicza 11, Kraków 30-345, Poland

KEYWORDS Magnetic properties, Phase transitions, Hysteresis, Gas adsorption, Irradiation

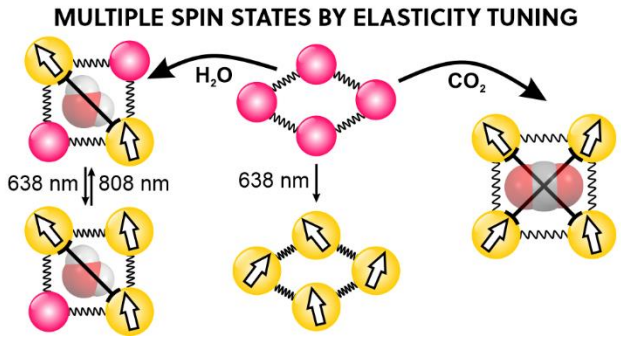

ABSTRACT: Iron(II) spin cross-over (SCO) compounds combine a thermally driven transition from the diamagnetic low-spin (LS) state to the paramagnetic high-spin (HS) state with a distinct change in the crystal lattice volume. Inversely, if the crystal lattice volume was modulated post-synthetically, the spin state of the compound could be tunable, resulting in the inverse effect for SCO. Herein, we demonstrate such a spin-state tuning in a breathing cyanido-bridged porous coordination polymer (PCP), where the volume change resulting from guest-induced gate-opening and -closing directly affects its spin state. We report a synthesis of the three-dimensional coordination framework $\{[Fe^{II}(4\text{-CNpy})_4]_2[W^{IV}(CN)_8]\cdot 4H_2O\}_n$ (**1·4H₂O**; 4-CNpy = 4-cyanopyridine), which demonstrates a SCO phenomenon characterized by strong elastic frustration. This leads to the 48 K wide hysteresis loop above 140 K, but below this temperature results in a very gradual and incomplete SCO transition. **1·4H₂O** was activated under mild conditions, producing the nonporous $\{[Fe^{II}(4\text{-CNpy})_4]_2[W^{IV}(CN)_8]\}_n$ (**1**) via a single-crystal-to-single-crystal process involving a 7.3% volume decrease, which shows complete and nonhysteretic SCO at $T_{1/2}$ = 93 K. The low-temperature photoswitching behavior in **1** and **1·4H₂O** manifested the characteristic elasticity of the frameworks; **1** can be quantitatively converted into a metastable HS state after 638 nm light irradiation, while the photoactivation of **1·4H₂O** is only partial. Furthermore, nonporous **1** adsorbed CO_2 molecules in a gated process, leading to $\{[Fe^{II}(4\text{-CNpy})_4]_2[W^{IV}(CN)_8]\cdot 4CO_2\}_n$ (**1·4CO₂**), which resulted in a 15% volume increase and stabilization of the HS state in the whole temperature range down to 2 K. The demonstrated post-synthetic guest-exchange employing common gases is an efficient approach for tuning spin state in breathing SCO-PCPs.

INTRODUCTION

Spin cross-over (SCO) phenomenon is a transition between low-spin (LS) and high-spin (HS) state of metal ions induced by a physical stimulus such as temperature, pressure, or light irradiation.[1] For octahedral iron(II) compounds in the solid state, a transition from the diamagnetic state to the paramagnetic S = 2 state is intertwined with the significant expansion of the crystal volume (Figure 1a), as well as the variation in optical and electric properties.[2-4] The simultaneous change of multiple properties makes SCO materials desirable for the nanofabrication of single-molecule junctions and thin films sensitive to environmental factors.[5-8] Although control over the spin state is usually achieved by temperature or mechanically, in their seminal work Kepert et al. demonstrated that the SCO properties can also be modulated with the uptake and release of the guest molecule in a porous coordination polymer (PCP).[9] The field expanded exponentially when Ohba et al. presented complete chemo-switching of the spin state in the Hofmann-type PCPs,[10, 11] and since then, numerous $Fe^{II}(L)[M^{II}(CN)_4]_n$ (M = Ni, Pt) compounds were reported to

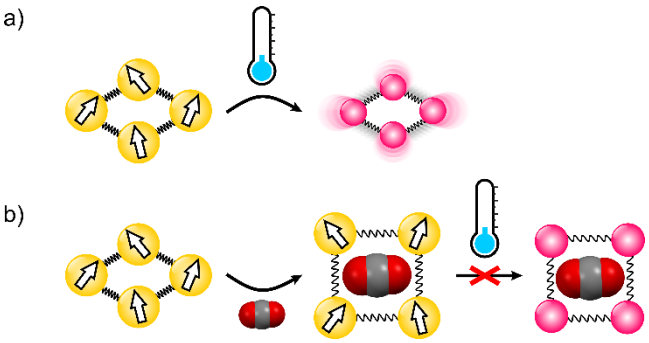

Figure 1. (a) Thermally induced high-spin to low-spin transition is typically associated with lattice contraction. (b) Volume expansion triggered by guest inclusion in the breathing coordination framework prevents spin transition to the small-volume low-spin state.

show the effect of the guest adsorption on SCO phenomenon.[12] While SCO frameworks show volume change resulting from the change in the spin state, large variation of crystal lattice volume upon guest uptake is also characteristic for PCPs which demonstrate the so-called "breathing" behavior.[13-16] As both SCO and guest-induced breathing result in crystal swelling/shrinking, one may expect that combination of these two phenomena would lead to a very strong coupling of these properties, that is, stabilization of the small-volume LS state for the closed-pore phase and the large-volume HS state in the open-pore phase (Figure 1). We expect that the crystal lattice volume closely associated with the spin state could be tuned by the kind of guest molecules being loaded into pores. This assumption is further supported by the pronounced effect of guest-induced gate-opening on the phase transition observed in donor-acceptor MOFs, reported recently by some of us.[17, 18] Noticeably, this phenomenon is hardly evidenced in rigid three-dimensional (3-D) Hofmann-type PCPs, in which strong host-guest interactions with guest molecules seem to overcome the volume change effect.[19-22] Thus in order to successfully observe the aforementioned coupling of the crystal lattice breathing with the spin transition, one should either decrease the strength of specific host-guest interactions or increase the volume change in the breathing SCO framework. The prospective candidate can be found in the family of octacyanidometallate-based compounds $\{[Fe^{II}(py)_4]_2[M^{IV}(CN)_8]\cdot xH_2O\}_n$ (py = pyridine derivatives, M = Mo, W, Nb, Re) [23], since some of us recently demonstrated large water-induced breathing of the octacyanomolybdate(IV) coordination polymer.[24] The impact of guest molecules on SCO properties of octacyanidometallate frameworks was mostly overlooked, with the exception of the water-induced spin transition reported by Song et al. in $\{[Fe^{II}((3\text{-pyridyl})methanol)_4]_2[W^{IV}(CN)_8]\cdot 4H_2O\}_n$.[25] Herein, we report $\{[Fe^{II}(4\text{-CNpy})_4]_2[W^{IV}(CN)_8]\}_n$ (1; 4-CNpy = 4-cyanopyridine), a flexible nonporous framework characterized by weakly cooperative spin transition at $T_{1/2}$ = 93 K. Upon adsorption of water molecules it showed a gate-opening breathing transition with a 7.3% increase of crystal volume resulting in $\{[Fe^{II}(4\text{-CNpy})_4]_2[W^{IV}(CN)_8]\cdot 4H_2O\}_n$ (1·4H₂O). The reorganization of the crystal framework led to the appearance of a 48 K wide hysteresis loop in the 187-235 K range, accompanied by strong elastic frustration, with the low-temperature phase showing mixed low-spin/high-spin state.

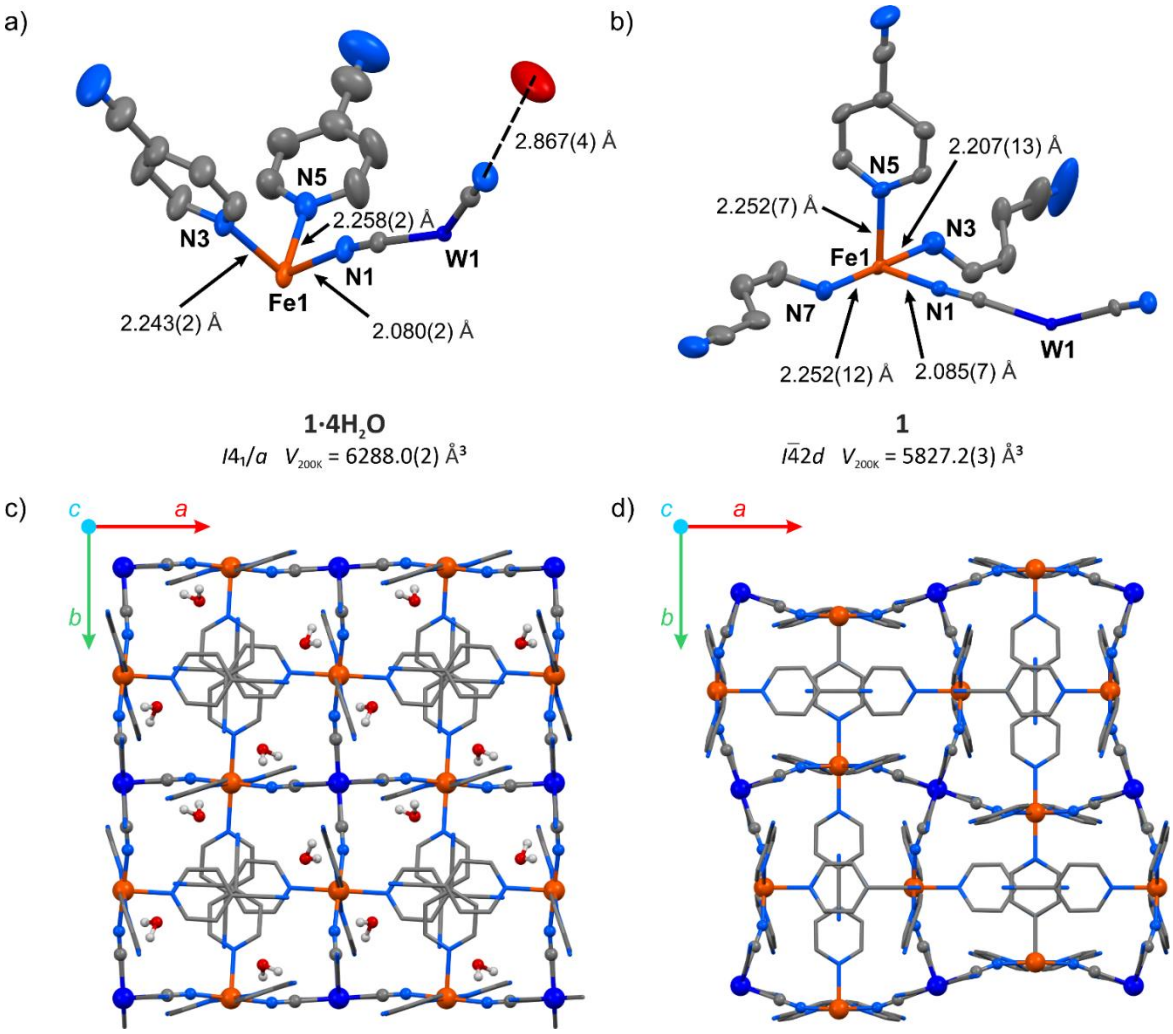

Figure 2. Structural transformation accompanying transition from **1·4H₂O** to **1**: asymmetric unit of **1·4H₂O** (a) and **1** (b) with selected bond distances (hydrogen atoms were omitted for clarity), as well as coordination frameworks of **1·4H₂O** (c) and **1** (d) as seen along crystallographic *c*-axis (hydrogen atoms of 4-cyanopyridine molecules were omitted for clarity). W – dark blue, Fe – orange, O – red, N – blue, C – grey.

The most striking feature of the nonporous **1** is the ability to accommodate four CO_2 molecules per formula unit in a gate-opening fashion, leading to the $\{[Fe^{II}(4\text{-}CNpy)_4][W^{IV}(CN)_8]\cdot 4CO_2\}_n$ (**1**·4CO_2). Finally, this CO_2 uptake resulted in a 15% increase in crystal volume, which in turn stabilized the HS state in the whole temperature range of 2-300 K. Herein, we demonstrate the total control of the spin state of a PCP driven by guest-dependent breathing-induced steric effects.

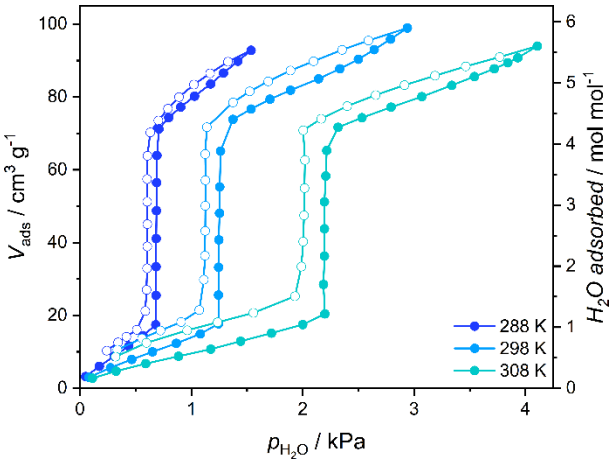

Figure 3. Vapor adsorption isotherms of water recorded for **1** (**1·4H₂O** activated in vacuum at 323 K). Full circles – adsorption, open circles – desorption.

RESULTS AND DISCUSSION

Crystal structures and water adsorption properties

The hydrated compound $\{[Fe^{II}(4\text{-}CNpy)_4]_2[W^{IV}(CN)_8]\cdot 4H_2O\}_n$ (**1·4H₂O**) was obtained as orange crystals by wet chemistry approach (see Experimental Section for details). It crystalized as a 3-D coordination network in a tetragonal crystal system, space group $I4_1/a$ (Table S1). All Fe(II) centers in the structure of **1·4H₂O** are surrounded by six nitrogen atoms and equivalent by symmetry. The iron(II) coordination sphere consists of four nitrogen atoms of aromatic 4-cyanopiridine rings and two cyanido ligands in a *trans* configuration (Figure 2a). The observed Fe-N bond lengths at 200 K are 2.080(2) Å for Fe-NC and 2.243(2) or 2.258(2) Å for Fe-$N_{pyridine}$, in line with expectations for iron(II) in a high-spin (HS) state.[25-34] Octacyanidotungstate(IV) forms four cyanide bridges with iron(II), leaving four terminal cyanides engaged in hydrogen bonding with water molecules with a CN···O distance of 2.867(5) Å (Table S2). Crystallization water molecules do not leave empty spaces in the framework (no void spaces were detected for 1.3 Å probe radius,[35] while the kinetic diameter of water is estimated to be 2.65 Å).[36] Noteworthy, the water molecules also form O···NC contact with the nitrogen atom belonging to the nitrile group of 4-cyanopyridine (3.074(7) Å). Despite the aromatic nature of the pyridine rings, no π-π interactions are observed, since all pyridine molecules are separated by more than 4 Å. However, 4-cyanopyridine molecules interact with each other through strongly polarized nitrile groups, which form -CN···C contacts characterized by the 3.244(5) Å intermolecular distance. Cooling the crystal of **1·4H₂O** below 190 K led to an immediate increase in crystal mosaicity and the disappearance of high-resolution (<1.0 Å) diffraction peaks and therefore the crystal structure could not be analyzed at lower temperatures.

Thermogravimetric analysis (TGA) performed on a powder sample of **1·4H₂O** under dry nitrogen flow shows an immediate decrease in mass already at room temperature (Figure S1). Within four minutes of measurement and below 30 °C, the mass reached a plateau of 96.5% m/m_0, and the sample mass remained constant up to 100 °C. This value is slightly higher than the expected m/m_0 = 94.9% for the completely dehydrated compound, because the dehydration starts immediately after removing the crystals from the mother solution at room temperature. The completeness of water removal is also supported by the powder X-ray diffraction pattern (PXRD) for the sample **1·4H₂O** activated in vacuum at room temperature, which does not show reflections of the parent **1·4H₂O** phase (Figure S2).

Following the TGA results, the single crystal of the hydrated framework **1·4H₂O** was dehydrated *in situ* by purging with dry nitrogen gas atmosphere at 343 K. The resulting anhydrous phase $\{[Fe^{II}(4\text{-}CNpy)_4]_2[W^{IV}(CN)_8]\}_n$ (**1**) was cooled and the sc-XRD measurement was performed at 200 K. Upon dehydration, the symmetry changes from $I4_1/a$ in **1·4H₂O** to $I\bar{4}2d$ in **1** and the unit cell volume is reduced by 7.3% (from 6288.0(2) Å³ for **1·4H₂O** to 5827.2(3) Å³ for **1**). In the dehydrated framework, there are four inequivalent nitrogen atoms coordinated to the Fe(II) center (Figure 2b), compared to three different Fe-N bonds in the hydrated form. The corresponding bond lengths are 2.085(7) Å for Fe-NC, and 2.207(13), 2.252(7) and 2.252(12) Å for Fe-$N_{pyridine}$, suggesting a fully HS state of Fe(II) at 200 K, similarly to the framework before dehydration. Importantly, as a result of water removal, the cyanido bridges underwent distinct bending, with the N-C-Fe angle changing from 170.8(2)° to 162.4(7)°. On the other hand, the equatorial pyridine coordination became more ordered, as $N_{pyridine1}$-Fe-$N_{pyridine2}$ angles change from 87.73(9)° and 92.27(9)° in **1·4H₂O** to 90.0(2)° in **1**. The aforementioned changes lead to the reorganization of the coordination skeleton as visible along the *c*-axis, which is depicted in the Figure 2c-d, with very little change observed along the *a*-axis (Figure S3). The selected bond lengths and angles in structures of **1·4H₂O** and **1** are summarized in Table S2. After complete evacuation of water guest molecules, the anhydrous **1** shows no cavities for the 1.3 Å radius probe molecule. This points to a breathing phenomenon, which can be described as a gate-closing process.[16, 37] Although gate-opening (GO) and gate-closing (GC) processes were recently demonstrated in amorphous[38] and microcrystalline[24, 39, 40] cyanido-bridged frameworks, to our knowledge the transition from **1·4H₂O** to **1** constitutes the first example of gate-closing visualized by single-crystal XRD in a coordination polymer featuring only cyanido bridges.

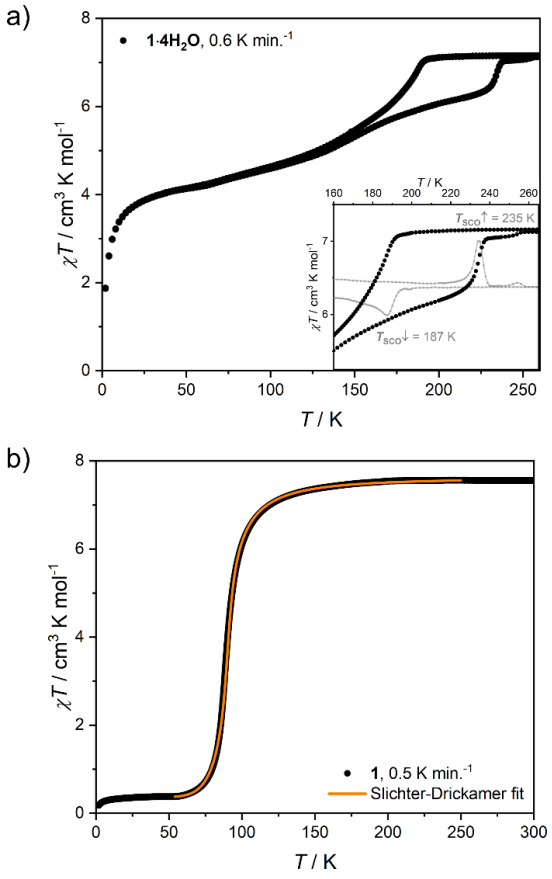

Figure 4. $\chi T(T)$ dependence recorded for **1·4H₂O** at $\mu_0 H_{dc}$ = 0.1 T (a) and close-up of the hysteresis loop with the corresponding d(χT)/dT derivative (inset), $\chi T(T)$ dependence recorded for **1** at $\mu_0 H_{dc}$ = 0.1 T and the fit of the Slichter-Drickamer model (Eq. 2) to the experimental data (b).

The gate-opening/closing character of the **1↔1·4H₂O** transformation is further confirmed by the measurement of volumetric adsorption of water vapor for **1** at 288-308 K (Figure 3). Adsorption curves up to the threshold water pressure can be classified as a type III isotherms typical for nonporous materials according to IUPAC[37], with approximately one water molecule per Fe_2W formula unit being adsorbed. However, a sudden increase in the amount of adsorbed vapor characteristic of GO can be observed above 40% relative humidity and the adsorbed volume after step-like increase corresponds to ca. 4.25 H_2O, almost perfectly in line with $\{[Fe^{II}(4\text{-}CNpy)_4]_2[W^{IV}(CN)_8]\cdot 4H_2O\}_n$ formulation deduced for **1·4H₂O** from sc-XRD measurement. A small further increase in adsorption occurs at higher vapor pressures. We attribute the difference between the total observed value and the expected value to the significant adsorption of water on the surface of crystals and the glass measurement tube. In the desorption branch, the adsorbed amount of water slowly decreases until it reaches 4.25 mol mol^{-1} around 35% relative humidity. Below this pressure, a stepwise decrease in the amount of adsorbed vapor corresponding to the GC process can be observed.

The pronounced structural transformation that accompanies the gate-opening breathing process leads to several changes in the infrared (IR) spectrum of **1** (Figure S4a). Water adsorption is accompanied by the appearance of a broad O-H stretching band in 2800-3700 cm^{-1} range and the H-O-H bending band at 1629 cm^{-1}, both confirming the presence of water molecules engaged in hydrogen bonding with cyanide ligands in the structure of **1·4H₂O**. Furthermore, the nitrile stretching bands change their structure (Figure S4b), with two unequal components at 2237 and 2241 cm^{-1} in the case of **1** reaching equal intensities at 2240 and 2247 cm^{-1} for **1·4H₂O**. This is correlated with three symmetrically independent 4-cyanopyridine molecules in the structure of **1**, as opposed to only two in **1·4H₂O**. All other 4-cyanopyridine vibrations in the fingerprint region shift by 2-3 cm^{-1} toward higher energies upon water adsorption, which is interpreted as general stiffening of the coordination skeleton.

*Magnetic properties of **1·4H₂O** and **1***

Structural data at 200 K are consistent with both **1·4H₂O** and **1** being composed of paramagnetic Fe(II) ions (S = 2). Consequently, **1·4H₂O** is characterized by magnetic susceptibility and temperature product (χT) of 7.16(11) cm^3 K mol^{-1} at 265 K (Figure 4a), which corresponds to two high-spin iron(II) centers per Fe_2W formula unit and the Landé factor g_{Fe} = 2.18(2). A relatively fast decrease of χT was observed below 192 K, at 140 K reaching 5.23 cm^3 K mol^{-1}. Below this point a decrease of χT was very gradual, reaching 4.19 cm^3 K mol^{-1} at 60 K (58.5% of the room temperature value). All changes of χT product at 192-60 K are attributed to the spin cross-over phenomenon, which is confirmed by Mössbauer spectroscopy measurements performed on cooling (Figure S5 and Table S3). A further decrease of χT below 60 K is unlikely to result from SCO, as the accompanying structural deformation rarely occurs at such low temperatures. However, it can be satisfactorily described with the following Hamiltonian constructed in the *PHI* software[41]:

$$\widehat{\boldsymbol{H}} = \boldsymbol{D}\left(\boldsymbol{S}_{\boldsymbol{z}}^{\boldsymbol{2}} - \boldsymbol{2}\right) + \boldsymbol{E}\left(\boldsymbol{S}_{\boldsymbol{x}}^{\boldsymbol{2}} - \boldsymbol{S}_{\boldsymbol{y}}^{\boldsymbol{2}}\right) + \boldsymbol{g}_{\mathbf{eff}}\boldsymbol{\beta}\vec{\boldsymbol{H}}\vec{\boldsymbol{S}} \quad \text{(EQUATION 1)}$$

with the additional intermolecular interaction parameter zJ. Fitting the model described above to the $\chi T(T)$ in the 2-50 K range and $M(H)$ at 2.0 K results in the following parameters: g_{eff}^2 = 7.61(1), D = 9.1(1) cm^{-1}, E = 2.5(1) cm^{-1} and zJ = -0.012(1) cm^{-1} (Figure S6). The D and E values obtained are within the expected range for high-spin iron(II) centers,[42-45] with a small zJ value resulting from HS Fe(II) being separated by long diamagnetic [-NC-$W^{IV}(CN)_6$-CN-] linkers, as well as LS Fe(II) centers. However, it should be noted that this procedure yields only approximate parameters for the HS iron(II) centers in **1·4H₂O**, as the g_{eff}^2 value in fact equals a molar fraction of HS iron(II) multiplied by the actual gyromagnetic ratio ($g_{eff}^2 = x_{HS}g_{Fe}^2$). This results from the fact that the amount of HS centers in 2-50 K range estimated from magnetic measurements is slightly higher than one Fe^{HS} per Fe_2W formula unit, and the results of Mössbauer measurements suggest that HS centers at low temperatures are not equivalent. The χT thermal dependence is reversible on heating to 140 K, when it starts to diverge from that recorded on cooling. At 230 K it reaches 6.43 cm^3 K mol^{-1}, which is much lower than the value of 7.16 cm^3 K mol^{-1} observed upon cooling. After this point, a stepwise increase of χT occurs up to 7.02 cm^3 K mol^{-1} at 238 K and the initial high-spin state is fully recovered above 256 K. This discrepancy of the cooling and heating processes manifests itself as a thermal hysteresis of SCO, with T_{sco} (defined as a maximum of the $d(\chi T)/dT$ derivative) equal to 187 K on cooling and 235 K on heating (Figure 4a, inset). The presence of the hysteresis loop was confirmed by Mössbauer spectroscopy (Figure S5) and dynamic scanning calorimetry (DSC; Figure S7). The simultaneous presence of a wide hysteresis loop above 180 K and an incomplete gradual transition below 140 K must result from elastic frustration of the framework.[46, 47] Because of the hysteretic behavior accounting only for 0.25-0.3 mol Fe per Fe_2W formula unit, as well as the rather blurred nature of the transition at 187 and 235 K, the signal intensity observed in the DSC measurement is relatively weak (Figure S7a,b). Because of that, the enthalpy of the transformation was determined only for the transition on heating. Depending on the background subtraction procedure (Figure S7c) and the assumed amount of SCO-active centers (0.25-0.3 per Fe_2W), the resulting transformation enthalpy is ΔH_{SCO} = 8.5-11.4 kJ mol^{-1} Fe, leading to ΔS_{SCO} = 38-51 J K^{-1} mol^{-1}.

Similarly to **1·4H₂O**, room temperature χT product observed for **1** equals 7.56(18) cm^3 K mol^{-1} (Figure 4b), as expected for two centers of high-spin iron(II) with g_{Fe} = 2.24(3) cm^3 K mol^{-1}. No change in χT is observed down to ca. 150 K, below which point the gradual decrease starts. Below 100 K a fast decrease occurs reaching 0.38 cm^3 K mol^{-1} at 50 K. The observed change represents 95% of the room temperature signal and is interpreted as a complete SCO transition, in line with the results of Mössbauer spectroscopy (Figure S8 and Table S4), which shows a pure HS state at 150 K and a pure LS state at 62 K. This points to-

wards weakly cooperative SCO transition that can be quantified with the Slichter-Drickamer model[48]:

$$k_B ln\left(\frac{1-\gamma_{HS}}{\gamma_{HS}}\right) = \Delta H_{HL} - T\Delta S_{HL} + \Gamma(1 - 2\gamma_{HS}) \qquad \text{(EQ. 2)}$$

Fitting the experimental χT curve in the 50-250 K range yields the following parameters: ΔH_{HL} = 4.74(3) kJ mol^{-1}, ΔS_{HL} = 51.0(3) J mol^{-1} K^{-1} and Γ = 1.12(1) kJ mol^{1} with R^2 = 0.99999. The determined SCO temperature T_{SCO} = $\Delta H_{HL}/\Delta S_{HL}$ = 93(1) K is very low, which for the ΔS_{HL} in the typical range (40-80 J K^{-1} mol^{-1})[49] must result from small ΔH_{HL}. Interestingly, unlike other SCO compounds that demonstrate spin transition below 100 K, which become kinetically trapped in the HS state due to the slow dynamics,[50-53] **1** demonstrates exactly the same SCO behavior also for a higher temperature sweep rate of 2 K min.$^{-1}$ (Figure S9). To further study the observed transition, we performed additional diffraction measurements at 140 K and 80 K. When **1** is cooled by 60 K from 200 K to 140 K, Fe-N bonds are shortened by 0.001-0.036 Å (on average 0.017(12) Å) for 4-cyanopiridine ligands and from 2.085(7) to 2.082(7) Å (0.003 Å) for nitrogen atoms belonging to cyanido ligands, which is mostly attributed to the thermal expansion. On the other hand, cooling by another 60 K down to 80 K leads to the much more distinct change of 0.112-0.221 Å (on average 0.17(4) Å) for 4-cyanopiridine and 0.125(7) Å for cyanido ligands, respectively. The sudden decrease of the bond length in the 140-80 K temperature range is in line with the transition temperature determined from magnetic and Mössbauer measurements, and the variation of the bond length is consistent with observations for other SCO frameworks featuring [Fe^{II}(py)$_4$(μ-NC)$_2$] moieties.[25-33] As the observed contraction of bond lengths falls in the typical range for similar assemblies, this raises the question about the source of unusually small ΔH_{HL}. This could be explained by stabilization of the HS state or destabilization of the LS state. No such effect can be identified by comparison of intermolecular interactions in the structures of **1** at 140 and 80 K (Table S2). Therefore, we hypothesize that a small value of ΔH_{HL} may result from the destabilizing effect of intermolecular repulsion in the low-spin state of **1**, which is expected to be sterically crowded, since the expanded high-spin state lacks void spaces.

Although both **1·4H$_2$O** and **1** share the same connectivity of the coordination skeleton, the above described SCO behavior of these two phases is very different. On the one side, **1·4H$_2$O** shows a 48 K wide hysteresis loop, unprecedented among octacyanidometallate-based SCO frameworks.[25-34, 54] This points to very high cooperativity of the system, but is accompanied by a relatively gradual χT change in the 60-140 K range in both the cooling and heating process. Interestingly, increasing the temperature sweep rate does not lead to a significant change in the width of the hysteresis loop (Figure S10), yet it decreases the total amount of iron(II) centers that undergo the SCO phenomenon. This suggests relatively slow kinetics of hysteretic SCO for **1·4H$_2$O** around 150 K, compared to the fast and gradual SCO observed for **1**, leading us to two conclusions. First, given the slightly cooperative nature of SCO in **1**, which comprises only [-NC-W^{IV}(CN)$_6$-CN-] bridges as elastic interaction pathways, elastic frustration of **1·4H$_2$O** must arise from the additional source of antiferroelastic interactions.[55] Most likely the appearance of hydrogen bonds increases cooperativity of the spin transition, but water molecules themselves act as stiff rods separating iron(II) centers. Taking into account the lack of free void spaces in the nonporous **1**, which accommodates water vapor only in the pore-opening transition, the steric effect of H$_2$O molecules must prevent the contraction of the framework to the full LS state. As a result, SCO for **1·4H$_2$O** is incomplete (representing approximately half iron(II) centers) at low temperatures. On the other side, the unusually fast kinetics of the SCO transition observed for **1** below 100 K suggests a high degree of structural flexibility, which is confirmed by observation of the pore-opening behavior induced by water vapor.

*Gas adsorption studies for **1***

Structural flexibility deduced for **1** from magnetic and vapor adsorption studies encouraged us to test its adsorption capability with other gas molecules. However, no gas adsorption was observed for N_2 and CO at 77 K, as well as NO at 121 K (Figure S11). On the other hand, at $T \geq$ 195 K, **1** shows stepped CO_2 adsorption (Figure 5a). The transition between nonporous and open-pore phase is almost binary, since no more than 5 cm^3 g^{-1} of carbon dioxide is adsorbed below the gate-opening pressure. The total volume of adsorbed CO_2 at 100 kPa reaches 62-68 cm^3 g^{-1} (in 205-194.7 K range), which corresponds to approximately 4 CO_2 molecules per Fe$_2$W formula unit. This amount is also reflected in the isobar measurements of CO_2 adsorption depicted in the Figure 5b. Thus, the formulation deduced for the CO_2-adsorbed phase from adsorption experiments is {[Fe^{II}(4-CNpy)$_4$]$_2$[W^{IV}(CN)$_8$]·4CO$_2$}$_n$ (**1·4CO$_2$**), very similar to the composition observed for**1·4H$_2$O** from sc-XRD. Powder X-ray diffraction measurements performed *in situ* under 100 kPa CO_2 on cooling show the disappearance of the parent phase **1** and the appearance of a new phase below 215 K (Figure S12), in line with the gas adsorption isobars. Similarly, the **1·4CO$_2$** starts to disappear at 230 K when heated, with concomitant restoration of **1**. This proves that only one crystal phase of **1·4CO$_2$** exists in the 200-300 K range. The reversibility of the transition from **1** to **1·4CO$_2$** was also tested by PXRD under isothermal conditions, with the powder pattern typical for **1** being restored by vacuum pumping of **1·4CO$_2$** (Figure S13). In order to determine thermodynamic parameters of these transitions, pressure-temperature points for a gate-opening and a gate-closing process determined from isotherms and isobars were fitted to the Clausius-Clapeyron relationship (Figure S14):

$$\mathbf{ln}\ (\boldsymbol{p}\ /\ \mathbf{kPa}) = \boldsymbol{A} + \frac{\Delta H_{trans}}{R}\frac{1}{T} \qquad \text{(EQ. 3)}$$

This approach results in A_{GO} = 19.1(5), ΔH_{GO} = -25.0(8) kJ mol^{-1} and A_{GC} = 16.8(4), ΔH_{GC} = -23.0(7) kJ mol^{-1}. These parameters were used to prepare the phase diagram of **1**/CO_2/**1·4CO$_2$** system presented in Figure 5c.

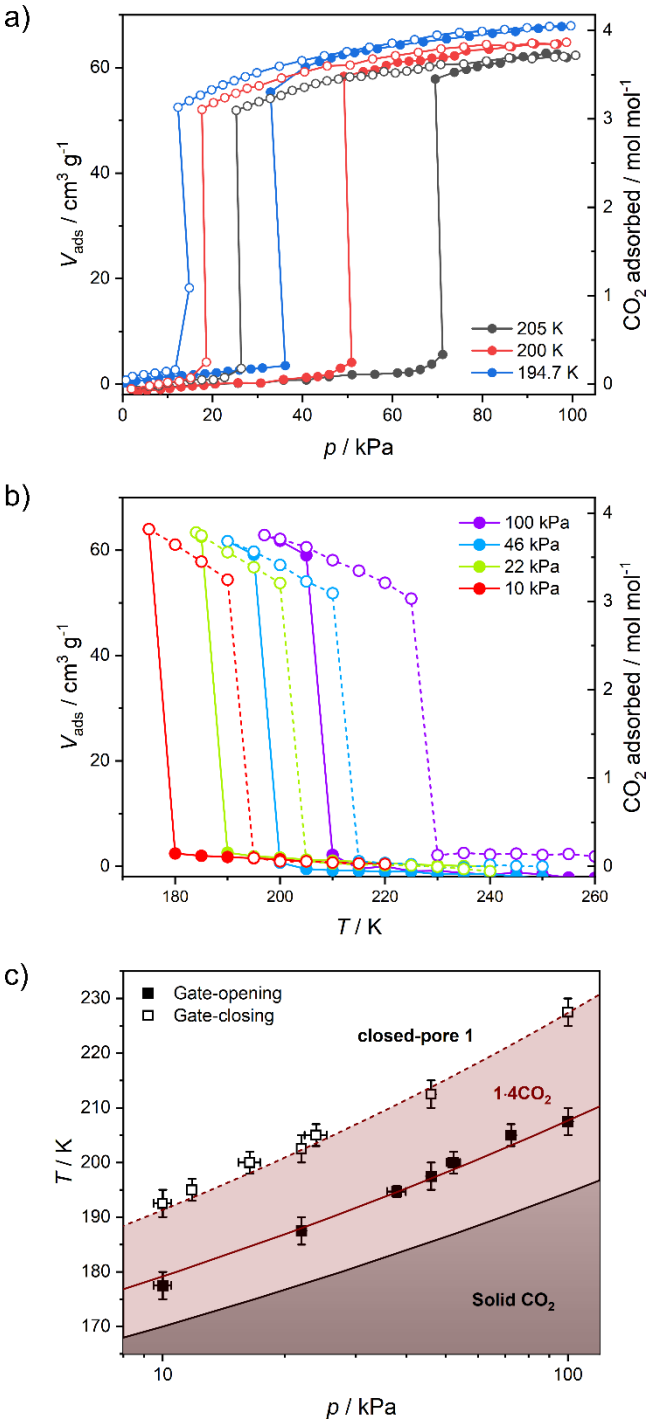

Figure 5. CO_2 adsorption in **1** studied as isotherms at different temperatures (a) and isobars at different CO_2 pressures (b), and phase diagram of **1**/CO_2/**1·4CO₂** system based on these results.

The powder X-ray diffraction pattern observed for **1·4CO₂** resembles the powder pattern of **1·4H₂O**, although with two apparent differences (Figure S15). All reflections are shifted towards lower 2θ values, suggesting even bigger expansion of the crystal lattice upon CO_2 adsorption as compared to the adsorption of H_2O. Furthermore, even though the powder patterns for **1·4CO₂** and **1·4H₂O** seem similar, many additional reflections are observed for the former (even after neglecting the remnant reflections of phase **1**, depicted in the Figure S13). Therefore, the powder pattern recorded for **1·4CO₂** at 200 K could not be indexed in the tetragonal crystal lattice. The unit cell search using *FOX* software[56] and the Le Bail refinement using *JANA2006* software[57] show good agreement for the orthorhombic cell (a = 20.364(3) Å, b = 19.950(3) Å, c = 16.461(3) Å with R_{wp} = 1.83%, Figure S16). Although these parameters are similar to the tetragonal cell observed for **1** at 200 K (Table S1), the expansion of the unit cell is observed in all the crystallographic directions and is anisotropic ($\Delta a/a$ = 6.1%, $\Delta b/b$ = 3.9% and $\Delta c/c$ = 4.1%). The total 14.8% volume expansion from **1** (V_{200K} = 5827.2(3) Å^3) to **1·4CO₂** (V_{200K} = 6687(3) Å^3), corresponds to 860 Å^3. For Z = 4 (as observed in **1** and **1·4H₂O**), this is in line with {[Fe^{II}(4-CNpy)$_4$]$_2$[W^{IV}(CN)$_8$]·4CO$_2$}$_n$ formulation, as 16 CO_2 molecules per formula unit are expected to occupy ≈744 Å^3.

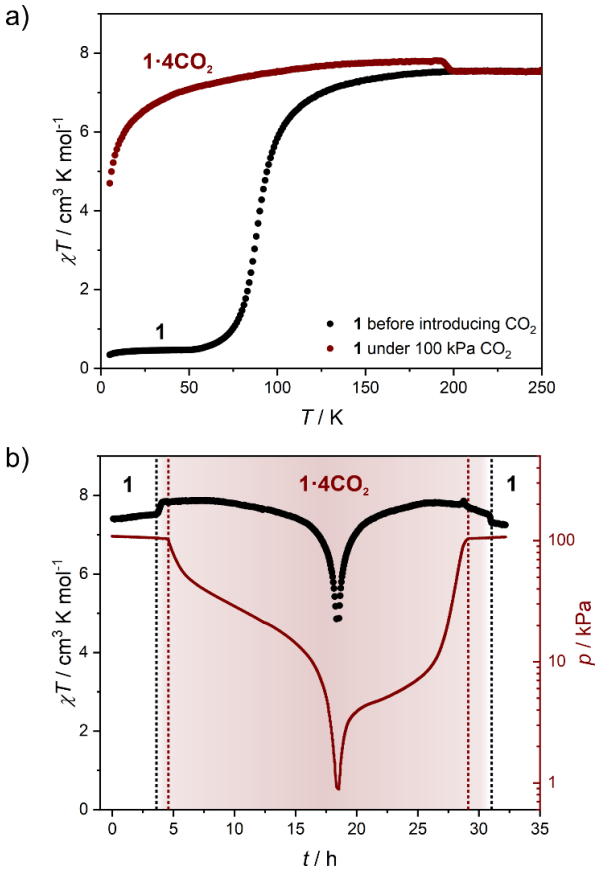

Figure 6. Magnetic studies of **1** performed during *in situ* CO_2 adsorption: thermal dependence of χT for **1** under 100 kPa He atmosphere (black points) and under 100 kPa CO_2 + 5 kPa He atmosphere (dark red line; average cooling rate 0.23 K min.$^{-1}$) (a), as well as time dependence of χT (black points) and total pressure (dark red line) (b). The zero point in the figure (b) corresponds to the start of the measurement depicted with dark red points in the figure (a). Dotted lines represent CO_2 adsorption/desorption effect (black) and CO_2 resublimation/sublimation (dark red).

In situ CO_2 adsorption IR and Raman studies

In order to better understand the host-guest interactions in the structure of **1·4CO₂**, we performed *in situ* IR and Raman spectroscopy studies under the CO_2 atmosphere.

Under *in situ* IR measurement conditions the octacyanidotungstate(IV) cyanide stretching mode is well visible (Figure S17). The small shift of this transition (≈4 cm^{-1}) after gate-opening is hard to explain on its own, while the very strong bands of gaseous CO_2 obscure the nitrile stretching bands of 4-cyanopyridine molecules. This issue is resolved by Raman spectroscopy measurement, in which no signal of gaseous CO_2 is observed in the 2300-2000 cm^{-1} range (Figure S18). The single broad peak of 4-cyanopyridine's nitrile can be observed in the Raman spectrum for **1** at 2239 cm^{-1}, which after CO_2 adsorption shifts to 2245 cm^{-1} in **1·4CO₂**. A similar change was observed in the IR spectrum of **1** after H_2O adsorption (Figure S4b), despite the fact that the water molecule only weakly interacts with the nitrile group - the 3.074(7) Å O···NC distance in the structure of **1·4H₂O** is 0.13 Å longer than typically observed for hydrogen bonds involving nitriles[58]. Therefore, the lack of more significant shifts in the Raman spectrum of **1·4CO₂**suggests that CO_2 molecules are not involved in any stronger interactions in this structure.

In situ CO_2 adsorption magnetic studies

The variation in magnetic properties of **1** upon *in situ* CO_2 adsorption was tested using a home-built gas cell (see Experimental section for details). A sample of **1·4H₂O** (14.9 mg) was activated inside the magnetometer chamber by 1 hour of vacuum pumping at 323 K and the gas cell was filled with 100 kPa He to facilitate good thermal contact. Then magnetic susceptibility was studied in the 250-5-250 K range (Figure 6a, black curve), which perfectly reproduces the behavior of the anhydrous **1** presented in the Figure 4b. Subsequently, the sample was heated to room temperature, the He pressure was reduced to 5 kPa (to maintain thermal conductivity at low temperatures) and 100 kPa CO_2 was introduced. This was followed by sample cooling to 250 K, and the magnetic susceptibility was studied again with an average temperature sweep rate of 0.23 K $min.^{-1}$. In the 250-200 K range the behavior of **1** is retained (Figure 6a, dark red curve), but when cooled from 200 K to 193 K the χT increases from 7.54 to 7.80 cm^3 K mol^{-1}. This is a direct result of the CO_2 adsorption and conversion of **1** to **1·4CO₂**, as evidenced in the Figure 5b, which demonstrates the pressure in system that was studied in real time. The stepwise χT increase induced by CO_2 adsorption is related to the small decrease in pressure (approximately 1.4 kPa), while the CO_2 resublimation that starts below 188 K results in a large continuous drop of pressure. The observed temperature range of adsorption in the magnetic measurement is downshifted by ≈10 K as compared to the isobar adsorption measurement under 100 kPa CO_2 (Figure 5b, purple line), which is the result of the slow kinetics of the gate-opening process. The appearance of this 3.4% increase of χT is expected to result from the variation in g_{Fe} resulting from the CO_2-induced framework expansion. The adsorption-related nature of this effect was additionally confirmed by the isothermal CO_2 introduction experiment at 195 K (Figure S19), in which no change in magnetic susceptibility is observed upon a fast pressure increase below 40 kPa CO_2, but a large variation of magnetization begins when the pressure increases above 50 kPa (in line with the phase diagram depicted in Figure 5c).

Cooling **1·4CO₂** below 190 K results in a very small change of χT (Figure 6a, dark red curve), which at 50 K equals 7.07 cm^3 K mol^{-1}. The minor decrease is expected to result from antiferromagnetic interactions between high-spin iron(II) centers and zero-field splitting effect. In order to minimize the last one, the sample was activated again at 323 K and the experiment was repeated under 50 kPa CO_2 (Figure S20; regeneration of the gate-closed **1** after activation was confirmed by repeated measurement of magnetic susceptibility under He atmosphere). The behavior of the sample under reduced pressure closely resembles that recorded under 100 kPa CO_2, but the transformation of **1** to **1·4CO₂** happens below 198 K instead of 200 K. Phase **1·4CO₂** under 50 kPa CO_2 was additionally characterized by the magnetization field dependence at several temperatures, and both $\chi T(T)$ and $M(H)$ curves were fitted using equation 1 (Figure S21). The experimental curves are well reproduced by the following set of parameters, assuming all iron(II) centers are in the high-spin state: g = 2.27(5), D = 9.0(1) cm^{-1}, E = 2.3(1) cm^{-1} and zJ = -0.085(1) cm^{-1}. The obtained values of D and E are reasonable for a HS iron(II) (and similar to those observed for **1·4H₂O**), which clearly confirms that the magnetic behavior of **1·4CO₂** can be properly described without assuming any degree of spin cross-over. At the same time zJ = -0.085(1) cm^{-1} for **1·4CO₂** is much larger than zJ = -0.012(1) cm^{-1} for **1·4H₂O**. This could be expected for the framework that contains only HS centers, as opposed to **1·4H₂O**, in which the HS sites are separated by

Table 1. Summary of SCO compounds showing CO_2 adsorption.

Compound	Type	Porosity	CO_2 adsorbed / mol mol^{-1} Fe	$\Delta V/V$	Impact on the SCO	Ref.
$Fe(pz)[Pt(CN)_4]$	2-D	microporous	1.1	n/a	none	10
$Fe(pz)[Ni(CN)_4]$	2-D	microporous	0.9	n/a	none	11
$[Fe(btzx)_3](ClO_4)_2$	1-D	microporous	0.9	<1%[a]	$\Delta T_{1/2}$ = +9 K [LS stabilized]	59
$[Fe(tpmd)(NCBH_3)_2]$	3-D	microporous	0.75-2.5	0.26%	$\Delta T_{1/2}$ = -29 K [HS stabilized]	60
$[Co(COO\text{-}terpy)_2]$	0-D	microporous/ gate-opening	1.2-2.0	1.6%	$\Delta T_{1/2} \approx$ +100 K[b] [LS stabilized]	61
$[Fe(4\text{-}CNpy)_4]_2[W(CN)_8]$ (**1**)	3-D	nonporous/ gate-opening	2.0	15%	HS only	This work

[a] 0.06% volume difference between CO_2-adsorbed phase studied at RT and activated phase studied at 240(2) K
[b] impossible to determine accurate value due to the very broad transition for the activated phase

diamagnetic LS sites.

The characterization described above led us to the conclusion that the adsorption of carbon dioxide in **1** quenches SCO and stabilizes the HS state in the whole 2-200 K temperature range. This type of behavior very rare among iron(II) spin cross-over compounds, and as far as we know was never observed with CO_2 as guest molecules. Although CO_2 adsorption in SCO compounds was previously reported in the literature, it was found to have negligible impact on the magnetic properties of Hofmann-type frameworks[10, 11] or lead to a small modulation of spin transition temperature in other compounds. [59, 60] The only exception was observed recently by Hayami et al. in a monomeric Co^{II} compound, where CO_2 adsorption stabilizes the LS state by strong intermolecular interactions. [61] The exceptional stabilization of the HS state in **1·4CO₂** is expected to originate from the large volume expansion resulting from CO_2-induced gate-opening (see Table 1). As deduced from X-ray diffraction, the introduction of H_2O into closed-pore **1** leads to the 7.9% volume expansion, while for CO_2 this effect is almost doubled with a 14.8% total volume increase. We speculate that this introduces the effect of "internal pressure" on iron(II) sites, with CO_2 molecules acting as long rigid rods, preventing network contraction associated with the spin transition. As such, this effect should not be restricted to CO_2 only, but would also be expected for other gas molecules adsorbed in the breathing frameworks. Although we did not observe breathing behavior for **1** under N_2, CO or NO atmosphere (Figure S11), we believe that this should inspire the search for other breathing SCO frameworks showing large volume change, as such frameworks could be utilized as highly selective sensors (as breathing frameworks are usually expected to show more selective gas adsorption than permanently microporous compounds,[16, 37] as demonstrated herein).

*Photomagnetic properties of **1** and **1·4H₂O***

The low-temperature elasticity of **1** and **1·4H₂O** was additionally tested by checking the possibility of inducing a high-spin state with visible light irradiation, the so-called Light-Induced Excited Spin State Trapping (LIESST) effect. [62] To allow for efficient irradiation and preserve the anhydrous state in the magnetometer chamber, the polycrystalline sample of **1** was crushed in the agate mortar and the 0.9 mg portion was sealed inside the polyethylene bag (all operations were carried out under argon atmosphere). The as-prepared sample reaches a slightly higher value of 1.15 cm^3 K mol^{-1} at 30 K, compared to 0.38 cm^3 K mol^{-1} in bulk (Figure 7a, black line). This may result from either increase in the number of defects after crystal crushing or from a partial sample decomposition during sealing the polyethylene bag with an impulse heat sealer. However, the phase identity as **1** is indubitably confirmed by the appearance of the same T_{SCO} as in bulk. Sample irradiation with λ = 638 nm at 10 K leads to a fast increase of magnetization, which saturates after 120 minutes (Figure S22). After turning off the light and sample thermalization back to 10 K (since constant light irradiation heats the sample by 2-3 K), the χT stabilizes at 6.28 cm^3 K mol^{-1} and shows no evolution in 20 minutes. This was followed by cooling the sample down to 2 K and χT measurement at the heating rate of 0.3 K min.$^{-1}$ (in order to accurately determine T_{LIESST}) [63, 64], as demonstrated in the Figure 7a (red line). The χT product reaches a maximum of 7.02 cm^3 K mol^{-1} at 35 K, which is very close to the 7.56 cm^3 K mol^{-1} observed at room temperature and therefore the LIESST for **1** is concluded to be almost quantitative. Furthermore, the T_{LIESST} determined for **1** as an extremum of d(χT)/dT equals 53 K (Figure S23), which in accordance with the formula proposed by Létard et al. [65] yields T_0 = 82 K. Despite the 3-D nature of the coordination skeleton in **1**, the T_0 value would classify it among iron(II) centers surrounded by six independent ligands. Both of these characteristics – the completeness of the photo-induced transition to the HS state and the low T_0

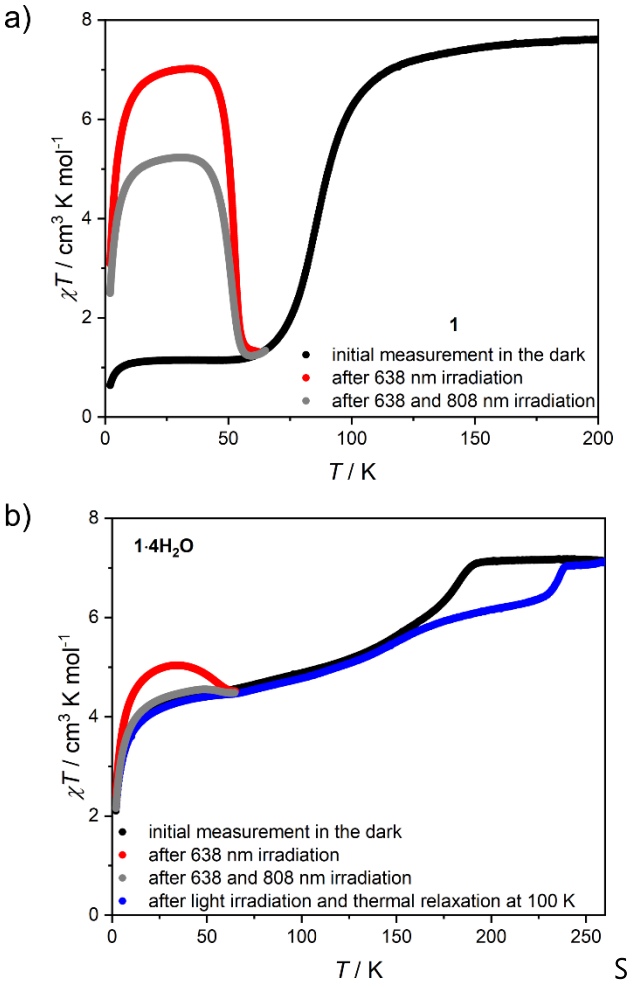

Figure 7. $\chi T(T)$ variation recorded after 638 and 808 nm light irradiation for **1** (a) and **1·4H₂O** (b). Initial measurements and measurement after thermal relaxation were performed at 2 K min.$^{-1}$ sweep rate, while measurements after light irradiation were performed at 0.3 K min.$^{-1}$.

value – further confirm the high degree of structural flexibility in **1**. Moreover, the photoinduced HS state in **1** at 10 K is rather persistent, as in the repeated experiment in which 638 nm was followed by 808 nm irradiation (Figure S24 and Figure 7a, gray line), the photo-induced χT was only decreased from 6.00 to 4.70 cm^3 K mol^{-1}. Therefore, the reverse-LIESST effect[66] triggered by λ = 808 nm light allows for deexcitation of only ≈25% metastable HS centers in **1**.

Phase **1·4H₂O** was prepared for photomagnetic measurements in a similar way to **1** – by sealing 1.1 mg crushed crystals inside the polyethylene bag, but with a very small amount of the mother solution, which allows for a perfect reproduction of the magnetic characteristics of the bulk sample (Figure 7b, black line). Irradiation of **1·4H₂O** with 638 nm light at 10 K leads to the immediate drop of χT due to the sample heating with light, which is followed by a small increase and saturation after 60 minutes (Figure S25). The χT product at 10 K changes from 3.64 cm^3 K mol^{-1} before irradiation to 4.57 cm^3 K mol^{-1} immediately after turning the light off, which drops to 4.48 cm^3 K mol^{-1} in 15 minutes. The same as **1**, this experiment was followed by cooling to 2 K and χT measurement with 0.3 K min.$^{-1}$ heating rate (Figure 7b, red line). The maximal observed value of 5.04 cm^3 K mol^{-1} at 35 K is well below the level of 7.16 cm^3 K mol^{-1} for the full HS phase. This makes LIESST for **1·4H₂O** quite inefficient, in line with previous conclusions on rigidity and slow dynamics of the framework at low temperature. Accordingly, the reverse-LIESST effect with 808 nm light is more effective with the photo-induced χT decreasing from 4.53 to 3.85 cm^3 K mol^{-1}, which accounts for ≈76% metastable HS centers (Figure S26 and Figure 7b, grey line). Surprisingly, the T_{LIESST} determined for **1·4H₂O** after 638 nm irradiation equals 55 K, very similar to **1** (Figure S27). This may be correlated with the presence of the LIESST effect only for those centers in the structure of **1·4H₂O** that undergo a spin transition in the temperature range close to the T_{SCO} in **1** (below 140 K). All the temperature-, light- and sorption-induced changes in the spin state of **1** were summarized in the Figure S28.

CONCLUSIONS

In search of three-dimensional breathing spin cross-over frameworks, we have prepared a coordination polymer $\{[Fe^{II}(4\text{-CNpy})_4]_2[W^{IV}(CN)_8]\}_n$ (**1**). It shows unusually low temperature of transition to the low spin state ($T_{1/2}$ = 93 K), resulting from a very small enthalpy change. Despite the low temperature of the structural transformation, the spin transition is complete and proceeds relatively fast (as compared to other compounds demonstrating low-temperature SCO). This results from extreme flexibility of the framework, which is confirmed by the observation of a gate-opening behavior induced by H_2O and CO_2 molecules. To our best knowledge, the transition between **1·4H₂O** and **1** is the first example of the gate-closing process studied by single-crystal XRD for a framework with only cyanides playing the role of a bridging ligand (without organic linkers). The breathing behavior resulting from water adsorption leads to the appearance of a 48 K wide hysteresis loop in case of **1·4H₂O**, unprecedented among other octacyanidometallate-based SCO compounds. More importantly, the inclusion of CO_2, which is assisted by an almost 15% volume expansion upon the transition from **1** to **1·4CO₂**, results in the stabilization of the high-spin state in the entire temperature range studied. This shows that rigid gas molecules can induce spin change in the spin cross-over framework not only by strong intermolecular interactions, but also by the "internal pressure" effect of volume expansion.

EXPERIMENTAL SECTION

Potassium octacyanotungstate(IV) dihydrate was obtained according to the reported procedure.[67] All other reagents were supplied by Sigma-Aldrich. Gases used for adsorption measurements were supplied by Nippon Sanso Holdings Corporation (He > 99.99995%, CO_2 > 99.995%).

Synthesis of $\{[Fe^{II}(4\text{-CNpy})_4]_2[W^{IV}(CN)_8]\cdot 4H_2O\}_n$ (1·4H₂O)

In the first vial $K_4[W^{IV}(CN)_8]\cdot 2H_2O$ (0.026 mmol, 15 mg) was dissolved in 8 mL H_2O, and in the second vial 4-cyanopyridine (9.0 mmol, 936 mg), Mohr's salt (0.048

mmol, 19 mg) and ascorbic acid (0.011 mmol, 2 mg) were dissolved in 24 mL H_2O with 15 minutes of sonication in the ultrasonic bath. Then both solutions were heated for 30 minutes at 36 °C in a water bath. Afterwards, a solution of octacyanotungstate(IV) was dropwise added to the iron(II) containing mixture with hand stirring. The resulting clear yellow mixture was left at 36 °C to crystalize. The red octahedral crystals that appeared after 48 hours were collected by filtration. Yield: 10 mg (30%). Purity was confirmed by elemental analysis and powder X-ray diffraction (Figure S2). Anal. Calcd for crystal structure ($C_{56}H_{40}Fe_2N_{24}O_4W$): C: 47.75%, N: 23.86%, H: 2,86%. Found: C: 48.72%, N: 24.38%, H: 2.57%. The discrepancy results from partial sample dehydration before the start of the measurement. Calcd for $C_{56}H_{37}Fe_2N_{24}O_{2.5}W$: C: 48.68%, C: 24.33%, H: 2.70%.

Single crystal X-ray diffraction

Sc-XRD experiments for **1·4H₂O** and **1** were performed using Bruker D8 Quest Eco diffractometer (Mo Kα sealed tube radiation source, Triumph® monochromator). Single crystals of **1·4H₂O** were moved directly from the mother liquor into NVH oil to avoid loss of the crystallization solvent. A single crystal of **1** was prepared *in situ* by heating **1·4H₂O** mounted on the goniometer head in the dry nitrogen stream using the Cryostream device (Oxford Cryosystems). Absorption corrections, data reduction and unit cell refinements were performed using SADABS and SAINT programs included in the Apex3 suite. The structures were solved using intrinsic phasing and refined anisotropically using weighted full-matrix least-squares on F^2.[68-70] Hydrogen atoms of the ligands were placed in calculated positions and refined as riding on the parent atoms. Structural diagrams were prepared using Mercury CSD 2020.3.0.[35] CCDC 2240344 (**1·4H₂O** at 200 K) and 2240345-2240347 (**1** at 200, 140 and 80 K, respectively) contain the supplementary crystallographic data for this paper. These data can be obtained free of charge via www.ccdc.cam.ac.uk/data_request/cif, or by emailing data_request@ccdc.cam.ac. uk, or by contacting The Cambridge Crystallographic Data Centre, 12 Union Road, Cambridge CB2 1EZ, UK; fax: +44 1223 336033.

Powder X-ray diffraction

PXRD data for phase purity confirmation (Figure S2) were obtained using Bruker D8 Advance diffractometer (Cu Kα radiation) at room temperature for ground crystalline samples of **1·4H₂O** loaded into glass capillaries under mother liquor (0.7 mm in diameter). Sample of **1** was obtained by drying **1·4H₂O** in vacuum ($p \approx 10^{-2}$ mbar) for 2 hours and inserted into glass capillary in oxygen- and water-free atmosphere of a glovebox (O_2 < 0.1 ppm, H_2O < 0.5 ppm) and sealed with silicone grease. Results were subjected to background correction using the DIFFRAC algorithm implemented in the DIFFRAC.EVA V5 software.

PXRD data for *in situ* CO_2 adsorption measurement were collected for samples in 0.5 mm diameter glass capillaries using Rigaku Ultima IV diffractometer (Cu Kα radiation). In order to allow vacuum treatment and CO_2 introduction, capillary was connected to stainless-steel (SUS) lines connected to a gas-handling system (BELSORP MAX; Microtrac BEL inc.). The temperature was controlled by a N_2 gas stream. Results were background corrected by subtracting the pattern recorded for the empty sample stage at room temperature. Unit cell for **1·4CO₂** was determined for the uncorrected measurement using FOX software, [56] and Le Bail refinement was performed in JANA2006 software.[57]

Volumetric adsorption measurements

The adsorption isotherm measurements were recorded on an automatic volumetric adsorption apparatus (BELSORP MAX; Microtrac BEL inc.) for ca. 25 mg sample of **1·4H₂O** activated by heating to 323 K under vacuum ($p \approx 10^{-4}$ mbar). For isotherm measurements of N_2 and CO at 77 K and CO_2 at 195 K, liquid nitrogen or dry ice/methanol bath were used. In the case of water vapor isotherm temperature was controlled using a water bath. For isobar measurements and isotherm measurement at different temperatures (including NO at 121 K), a home-built cryostat (ULVAC-Cryo) was utilized.

Spectroscopic measurements

Infrared spectra for **1·4H₂O** were recorded using a Nicolet iN10 MX FT-IR microscope in transmission mode (a small amount of powdered sample was spread on a BaF_2 pellet). Sample of **1** was obtained by *in situ* dehydration of **1·4H₂O** with dry nitrogen purge inside a Linkam THMS350V temperature controlled stage. *In situ* CO_2 adsorption was studied using JASCO FT/IR-4200 spectrometer for the sample of **1** mixed with KBr and dispersed in between two CaF_2 windows inside the cryostat (RC102, CRYO industries) connected to a gas-handling and pressure monitoring system (BELSORP MAX, Microtrac BEL inc.). Raman spectra during *in situ* CO_2 adsorption were studied using JASCO NRS-4500 Raman microscope using a cryostat system (RC102, CRYO Industries) connected with a gas-handling and pressure-monitoring system (BELSOR MAX, Microtrac BEL inc.). Quartz and CaF_2 were equipped over the sample room and the vacuum insulating shield of the cryostat, respectively. The sample was inspected using an objective lens (Olympus SLMPLN20x) and was irradiated with a 532 nm Raman excitation laser. The transmission ^{57}Fe Mössbauer spectra were collected using a Wissel spectrometer with a bath liquid nitrogen cryostat. Polycrystalline sample of **1·4H₂O** (ca. 50 mg) was inserted into a polyethylene (PE) bag with a mother liquor to prevent its dehydration and sealed using an impulse heat sealer. Sample of **1** (ca. 50 mg) was obtained by drying **1·4H₂O** in vacuum ($p \approx 10^{-2}$ mbar) for 2 hours, and then sealed inside PE bag in oxygen- and water-free atmosphere of a glovebox (O_2 < 0.1 ppm, H_2O < 0.5 ppm). The samples were mounted for the measurements inside a copper ring. Mössbauer spectra were fitted with the use of WinNormos-for-Igor software package, assuming Lorentzian shape of the resonance lines. In case of **1·4H₂O** two additional doublets (with a large value of quadrupole splitting) originating from the iron species in solution were included to improve quality of the fits. Those signals (marked with purple asterisks in the Figure S5) were excluded from the calculation of the relative fractions of different iron(II) forms in the solid,

which were determined from the ratio of the areas of the corresponding doublets attributed to **1·4H₂O**.

Magnetic and photomagnetic measurements

Magnetic and photomagnetic studies for **1** and **1·4H₂O** were performed using a Quantum Design MPMS-3 Evercool magnetometer in magnetic fields up to 7 T. Polycrystalline sample of **1·4H₂O** (10.9 mg) was inserted into a polyethylene (PE) bag with a minimal amount of mother liquor and sealed using an impulse heat sealer. Sample of **1** (8.6 mg) was obtained by drying **1·4H₂O** in vacuum ($p \approx 10^{-2}$ mbar) for 2 hours, and then sealed inside PE bag in oxygen- and water-free atmosphere of a glovebox (O_2 < 0.1 ppm, H_2O < 0.5 ppm). Both samples were mounted onto the quartz sample holder using Kapton tape. The experimental data were corrected for the diamagnetism of the sample. Samples were prepared for photomagnetic measurements in the PE bags in a similar manner, but only small amount (ca. 1 mg) was used, and PE bags were placed between two layers of adhesive tape (5 mm diameter) and inserted into the plastic straw. Irradiation was performed using laser diodes (power at the sample position 10-20 mW/cm²). Diamagnetic corrections were determined by comparison with bulk measurements.

In situ CO_2 adsorption magnetic measurements

Magnetic susceptibility measurements under CO_2 atmosphere were performed using a Quantum Design MPMS-XL on a polycrystalline sample of **1·4H₂O** (ca. 15 mg), which was placed inside the gelatin capsule with ca. 100 mg of polyester wool to ensure its immobilization. The capsule was pierced with a needle and placed inside a straw, which was attached to the home-built SUS (stainless steel) sample rod described elsewhere.[18] The SUS tube was connected to the gas-handling system (BELSORP MAX; Microtrac BEL inc.). The sample was activated *in situ* by heating it to 323 K and vacuum pumping ($p \approx 10^{-4}$ mbar). Measurements for the sample in the activated state (**1**) were performed under 100 kPa He to ensure good thermal contact of the sample with the magnetometer cavity. Measurements for **1** under CO_2 atmosphere were performed with an additional 5 kPa He in the system, in order to preserve thermal conductivity after complete CO_2 resublimation. The connection of the SUS sample rod to the gas-handling system was left open for the entire measurement time in order to enable constant monitoring of the gas pressure in the system. All the measurements were conducted in the temperature stabilization mode. Diamagnetic corrections were determined by comparison of the measurement for activated **1** with the bulk measurement for **1** in the PE bag.

Additional measurements

TGA was performed using a NETZSCH TG 209 F1 Libra under a flow of nitrogen (20 mL $min.^{-1}$) and a temperature scanning rate of 2 °C $min.^{-1}$. DSC was performed using a NETZSCH DSC214 Polyma for the sample in a closed-lid sample holder at a temperature sweep rate of 5 K $min.^{-1}$. Elemental analyzes were performed using an ELEMENTAR Vario Micro Cube CHNS analyzer.

ASSOCIATED CONTENT

Supporting Information. TGA plot, powder X-ray diffraction patterns, additional structural information, additional magnetic and photomagnetic data, additional adsorption data, and spectroscopic data (IR, Raman, Mössbauer) are available free of charge via the Internet at http://pubs.acs.org.

AUTHOR INFORMATION

Corresponding Author

*michal.magott@uj.edu.pl
*miyasaka@imr.tohoku.ac.jp
*dawid.pinkowicz@uj.edu.pl

Author Contributions

All authors have given approval to the final version of the manuscript.
‡These authors contributed equally.

ACKNOWLEDGMENT

This work was financed by the Polish National Science Centre within the OPUS 20 (2020/39/B/ST5/02815) project and a Grant-in-Aid for Scientific Research (Nos. 20H00381, 21K18925, 21H01900, and 22H00324) from MEXT, Japan.. MM gratefully acknowledges Polish Agency for Academic Exchange within the BEKKER scholarship (BEK/2021/1/00178).

REFERENCES

(1) Gütlich, P.; Garcia, Y.; Goodwin, H. A. Spin crossover phenomena in Fe(II) complexes. *Chem. Soc. Rev.* **2000**, *29* (6), 419-427.
(2) Brooker, S. Spin crossover with thermal hysteresis: practicalities and lessons learnt. *Chem. Soc. Rev.* **2015**, *44* (10), 2880-2892.
(3) Decurtins, S.; Gutlich, P.; Hasselbach, K. M.; Hauser, A.; Spiering, H. Light-induced excited-spin-state trapping in iron(II) spin-crossover systems. Optical spectroscopic and magnetic susceptibility study. *Inorg. Chem.* **1985**, *24* (14), 2174-2178.
(4) Rotaru, A.; Gural'skiy, I. y. A.; Molnár, G.; Salmon, L.; Demont, P.; Bousseksou, A. Spin state dependence of electrical conductivity of spin crossover materials. *Chem. Commun.* **2012**, *48* (35), 4163-4165.
(5) Miyamachi, T.; Gruber, M.; Davesne, V.; Bowen, M.; Boukari, S.; Joly, L.; Scheurer, F.; Rogez, G.; Yamada, T. K.; Ohresser, P.; et al. Robust spin crossover and memristance across a single molecule. *Nat. Commun.* **2012**, *3* (1), 938.
(6) Aravena, D.; Ruiz, E. Coherent Transport through Spin-Crossover Single Molecules. *J. Am. Chem. Soc.* **2012**, *134* (2), 777-779.
(7) Poggini, L.; Milek, M.; Londi, G.; Naim, A.; Poneti, G.; Squillantini, L.; Magnani, A.; Totti, F.; Rosa, P.; Khusniyarov, M. M.; et al. Room temperature control of spin states in a thin film of a photochromic iron(ii) complex. *Mater. Horiz.* **2018**, *5* (3), 506-513.
(8) Kumar, K. S.; Ruben, M. Sublimable Spin-Crossover Complexes: From Spin-State Switching to Molecular Devices. *Angew. Chem. Int. Ed.* **2021**, *60* (14), 7502-7521.
(9) Halder, G. J.; Kepert, C. J.; Moubaraki, B.; Murray, K. S.; Cashion, J. D. Guest-Dependent Spin Crossover in a Nanoporous Molecular Framework Material. *Science* **2002**, *298* (5599), 1762-1765.

(10) Ohba, M.; Yoneda, K.; Agustí, G.; Muñoz, M. C.; Gaspar, A. B.; Real, J. A.; Yamasaki, M.; Ando, H.; Nakao, Y.; Sakaki, S.; et al. Bidirectional Chemo-Switching of Spin State in a Microporous Framework. *Angew. Chem. Int. Ed.* **2009**, *48* (26), 4767-4771.
(11) Southon, P. D.; Liu, L.; Fellows, E. A.; Price, D. J.; Halder, G. J.; Chapman, K. W.; Moubaraki, B.; Murray, K. S.; Létard, J.-F.; Kepert, C. J. Dynamic Interplay between Spin-Crossover and Host−Guest Function in a Nanoporous Metal−Organic Framework Material. *J. Am. Chem. Soc.* **2009**, *131* (31), 10998-11009.
(12) Ni, Z.-P.; Liu, J.-L.; Hoque, M. N.; Liu, W.; Li, J.-Y.; Chen, Y.-C.; Tong, M.-L. Recent advances in guest effects on spin-crossover behavior in Hofmann-type metal-organic frameworks. *Coord. Chem. Rev.* **2017**, *335*, 28-43.
(13) Serre, C.; Millange, F.; Thouvenot, C.; Noguès, M.; Marsolier, G.; Louër, D.; Férey, G. Very Large Breathing Effect in the First Nanoporous Chromium(III)-Based Solids: MIL-53 or $Cr^{III}(OH)\cdot\{O_2C-C_6H_4-CO_2\}\cdot\{HO_2C-C_6H_4-CO_2H\}_x\cdot H_2O_y$. *J. Am. Chem. Soc.* **2002**, *124* (45), 13519-13526.
(14) Mellot-Draznieks, C.; Serre, C.; Surblé, S.; Audebrand, N.; Férey, G. Very Large Swelling in Hybrid Frameworks: A Combined Computational and Powder Diffraction Study. *J. Am. Chem. Soc.* **2005**, *127* (46), 16273-16278.
(15) Horike, S.; Shimomura, S.; Kitagawa, S. Soft porous crystals. *Nat. Chem.* **2009**, *1* (9), 695-704.
(16) Schneemann, A.; Bon, V.; Schwedler, I.; Senkovska, I.; Kaskel, S.; Fischer, R. A. Flexible metal–organic frameworks. *Chem. Soc. Rev.* **2014**, *43* (16), 6062-6096.
(17) Kosaka, W.; Liu, Z.; Zhang, J.; Sato, Y.; Hori, A.; Matsuda, R.; Kitagawa, S.; Miyasaka, H. Gas-responsive porous magnet distinguishes the electron spin of molecular oxygen. *Nat. Commun.* **2018**, *9* (1), 5420.
(18) Zhang, J.; Kosaka, W.; Kitagawa, Y.; Miyasaka, H. A metal–organic framework that exhibits CO2-induced transitions between paramagnetism and ferrimagnetism. *Nat. Chem.* **2021**, *13* (2), 191-199.
(19) Murphy, M. J.; Zenere, K. A.; Ragon, F.; Southon, P. D.; Kepert, C. J.; Neville, S. M. Guest Programmable Multistep Spin Crossover in a Porous 2-D Hofmann-Type Material. *J. Am. Chem. Soc.* **2017**, *139* (3), 1330-1335.
(20) Turo-Cortés, R.; Bartual-Murgui, C.; Castells-Gil, J.; Muñoz, M. C.; Martí-Gastaldo, C.; Real, J. A. Reversible guest-induced gate-opening with multiplex spin crossover responses in two-dimensional Hofmann clathrates. *Chem. Sci.* **2020**, *11* (41), 11224-11234.
(21) Xue, J.-P.; Hu, Y.; Zhao, B.; Liu, Z.-K.; Xie, J.; Yao, Z.-S.; Tao, J. A spin-crossover framework endowed with pore-adjustable behavior by slow structural dynamics. *Nat. Commun.* **2022**, *13* (1), 3510.
(22) Orellana-Silla, A.; Turo-Cortés, R.; Rubio-Giménez, V.; Bartual-Murgui, C.; Ameloot, R.; Martí-Gastaldo, C.; Muñoz, M. C.; Real Cabezos, J. A. A. Broad-range spin-crossover modulation in guest-responsive 2D Hofmann-type coordination polymers. *Inorg. Chem. Front.* **2023**, *10*, 600-611.
(23) Chorazy, S.; Zakrzewski, J. J.; Magott, M.; Korzeniak, T.; Nowicka, B.; Pinkowicz, D.; Podgajny, R.; Sieklucka, B. Octacyanidometallates for multifunctional molecule-based materials. *Chem. Soc. Rev.* **2020**, *49* (16), 5945-6001.
(24) Magott, M.; Gaweł, B.; Sarewicz, M.; Reczyński, M.; Ogorzały, K.; Makowski, W.; Pinkowicz, D. Large breathing effect induced by water sorption in a remarkably stable nonporous cyanide-bridged coordination polymer. *Chem. Sci.* **2021**, *12*, 9176-9188.
(25) Wei, R.-M.; Kong, M.; Cao, F.; Li, J.; Pu, T.-C.; Yang, L.; Zhang, X.-L.; Song, Y. Water induced spin-crossover behaviour and magneto-structural correlation in octacyanotungstate(iv)-based iron(ii) complexes. *Dalton Trans.* **2016**, *45* (46), 18643-18652.
(26) Arai, M.; Kosaka, W.; Matsuda, T.; Ohkoshi, S.-i. Observation of an Iron(II) Spin-Crossover in an Iron Octacyanoniobate-Based Magnet. *Angew. Chem. Int. Ed.* **2008**, *47* (36), 6885-6887.
(27) Ohkoshi, S.-i.; Imoto, K.; Tsunobuchi, Y.; Takano, S.; Tokoro, H. Light-induced spin-crossover magnet. *Nat. Chem.* **2011**, *3* (7), 564-569.
(28) Ohkoshi, S.-i.; Takano, S.; Imoto, K.; Yoshikiyo, M.; Namai, A.; Tokoro, H. 90-degree optical switching of output second-harmonic light in chiral photomagnet. *Nat. Photonics* **2014**, *8* (1), 65-71.
(29) Imoto, K.; Ohkoshi, S.-i. Photoreversible Spin-crossover Ferrimagnetism in Fe2[Nb(CN)8](4-methylpyridine)8·2H2O. *Chem. Lett.* **2016**, *45* (3), 359-361.
(30) Kawabata, S.; Chorazy, S.; Zakrzewski, J. J.; Imoto, K.; Fujimoto, T.; Nakabayashi, K.; Stanek, J.; Sieklucka, B.; Ohkoshi, S.-i. In Situ Ligand Transformation for Two-Step Spin Crossover in $Fe^{II}[M^{IV}(CN)_8]^{4-}$ (M = Mo, Nb) Cyanido-Bridged Frameworks. *Inorg. Chem.* **2019**, *58* (9), 6052-6063.
(31) Chorazy, S.; Charytanowicz, T.; Pinkowicz, D.; Wang, J.; Nakabayashi, K.; Klimke, S.; Renz, F.; Ohkoshi, S.-i.; Sieklucka, B. Octacyanidorhenate(V) Ion as an Efficient Linker for Hysteretic Two-Step Iron(II) Spin Crossover Switchable by Temperature, Light, and Pressure. *Angew. Chem. Int. Ed.* **2020**, *59* (36), 15741-15749.
(32) Charytanowicz, T.; Zakrzewski, J. J.; Dziedzic-Kocurek, K.; Chorazy, S.; Sieklucka, B. The ON–OFF switching of thermal spin crossover by interstitial solvent exchange in a layered Re^{V}–CN–Fe^{II} coordination framework. *J. Appl. Phys.* **2021**, *129* (14), 143902.
(33) Kawabata, S.; Nakabayashi, K.; Imoto, K.; Ohkoshi, S.-i. Spin crossover phenomenon in a three-dimensional cyanido-bridged Fe^{II}–Mo^{IV} assembly. *J. Appl. Phys.* **2021**, *129* (10), 105501.
(34) Kosaka, W.; Tokoro, H.; Matsuda, T.; Hashimoto, K.; Ohkoshi, S.-i. Extremely Gradual Spin-Crossover Phenomenon in a Cyano-Bridged Fe−Mo Bimetallic Assembly. *J. Phys. Chem. C* **2009**, *113* (35), 15751-15755.
(35) Macrae, C. F.; Sovago, I.; Cottrell, S. J.; Galek, P. T. A.; McCabe, P.; Pidcock, E.; Platings, M.; Shields, G. P.; Stevens, J. S.; Towler, M.; et al. Mercury 4.0: from visualization to analysis, design and prediction. *J. Appl. Crystallogr.* **2020**, *53* (1), 226-235.
(36) Ismail, A. F.; Khulbe, K. C.; Matsuura, T. *Gas Separation Membranes: Polymeric and Inorganic*; Springer, 2015.
(37) Yaghi, O. M.; Kalmutzki, M. J.; Diercks, C. S. *Introduction to Reticular Chemistry: Metal-Organic Frameworks and Covalent Organic Frameworks*; Wiley-VCH Verlag GmbH & Co. KGaA, 2019.
(38) Yoshino, H.; Yamagami, K.; Wadati, H.; Yamagishi, H.; Setoyama, H.; Shimoda, S.; Mishima, A.; Le Ouay, B.; Ohtani, R.; Ohba, M. Coordination Geometry Changes in Amorphous Cyanide-Bridged Metal–Organic Frameworks upon Water Adsorption. *Inorg. Chem.* **2021**, *60* (5), 3338-3344.
(39) Hibble, S. J.; Chippindale, A. M.; Pohl, A. H.; Hannon, A. C. Surprises from a Simple Material—The Structure and Properties of Nickel Cyanide. *Angew. Chem. Int. Ed.* **2007**, *46* (37), 7116-7118.
(40) Alowasheeir, A.; Tominaka, S.; Ide, Y.; Yamauchi, Y.; Matsushita, Y. Two-dimensional cyano-bridged coordination polymer of $Mn(H_2O)_2[Ni(CN)_4]$: structural analysis and proton conductivity measurements upon dehydration and rehydration. *CrystEngComm* **2018**, *20* (42), 6713-6720.
(41) Chilton, N. F.; Anderson, R. P.; Turner, L. D.; Soncini, A.; Murray, K. S. PHI: A powerful new program for the analysis of

anisotropic monomeric and exchange-coupled polynuclear d- and f-block complexes. *J. Comput. Chem.* **2013**, *34* (13), 1164-1175.
(42) Boča, R. Zero-field splitting in metal complexes. *Coord. Chem. Rev.* **2004**, *248* (9), 757-815.
(43) Ozarowski, A.; Zvyagin, S. A.; Reiff, W. M.; Telser, J.; Brunel, L.-C.; Krzystek, J. High-Frequency and -Field EPR of a Pseudo-octahedral Complex of High-Spin Fe(II): Bis(2,2‘-bi-2-thiazoline)bis(isothiocyanato)iron(II). *J. Am. Chem. Soc.* **2004**, *126* (21), 6574-6575.
(44) Novitchi, G.; Jiang, S.; Shova, S.; Rida, F.; Hlavička, I.; Orlita, M.; Wernsdorfer, W.; Hamze, R.; Martins, C.; Suaud, N.; et al. From Positive to Negative Zero-Field Splitting in a Series of Strongly Magnetically Anisotropic Mononuclear Metal Complexes. *Inorg. Chem.* **2017**, *56* (24), 14809-14822.
(45) Magott, M.; Ceglarska, M.; Rams, M.; Sieklucka, B.; Pinkowicz, D. Magnetic interactions controlled by light in the family of Fe(II)–M(IV) (M = Mo, W, Nb) hybrid organic–inorganic frameworks. *Dalton Trans.* **2022**, *51* (22), 8885-8892.
(46) Nishino, M.; Boukheddaden, K.; Konishi, Y.; Miyashita, S. Simple Two-Dimensional Model for the Elastic Origin of Cooperativity among Spin States of Spin-Crossover Complexes. *Phys. Rev. Lett.* **2007**, *98* (24), 247203.
(47) Paez-Espejo, M.; Sy, M.; Boukheddaden, K. Elastic Frustration Causing Two-Step and Multistep Transitions in Spin-Crossover Solids: Emergence of Complex Antiferroelastic Structures. *J. Am. Chem. Soc.* **2016**, *138* (9), 3202-3210.
(48) Slichter, C. P.; Drickamer, H. G. Pressure-Induced Electronic Changes in Compounds of Iron. *J. Chem. Phys.* **1972**, *56* (5), 2142-2160.
(49) Nicolazzi, W.; Bousseksou, A. Thermodynamical aspects of the spin crossover phenomenon. *C. R. Chim.* **2018**, *21* (12), 1060-1074.
(50) Bousseksou, A.; Verelst, M.; Constant-Machado, H.; Lemercier, G.; Tuchagues, J.-P.; Varret, F. $[Fe^{II}(TRIM)_2]F_2$, the First Example of Spin Conversion Monitored by Molecular Vibrations. *Inorg. Chem.* **1996**, *35* (1), 110-115.
(51) Milin, E.; Patinec, V.; Triki, S.; Bendeif, E.-E.; Pillet, S.; Marchivie, M.; Chastanet, G.; Boukheddaden, K. Elastic Frustration Triggering Photoinduced Hidden Hysteresis and Multistability in a Two-Dimensional Photoswitchable Hofmann-Like Spin-Crossover Metal–Organic Framework. *Inorg. Chem.* **2016**, *55* (22), 11652-11661.
(52) Ndiaye, M. M.; Pillet, S.; Bendeif, E.-E.; Marchivie, M.; Chastanet, G.; Boukheddaden, K.; Triki, S. Hidden Hysteretic Behavior of a Paramagnetic Iron(II) Network Revealed by Light Irradiation. *Eur. J. Inorg. Chem.* **2018**, *2018* (3-4), 305-313.
(53) Ye, Y. S.; Chen, X. Q.; De Cai, Y.; Fei, B.; Dechambenoit, P.; Rouzières, M.; Mathonière, C.; Clérac, R.; Bao, X. Slow Dynamics of the Spin-Crossover Process in an Apparent High-Spin Mononuclear FeII Complex. *Angew. Chem. Int. Ed.* **2019**, *58* (52), 18888-18891.
(54) Pinkowicz, D.; Rams, M.; Mišek, M.; Kamenev, K. V.; Tomkowiak, H.; Katrusiak, A.; Sieklucka, B. Enforcing Multifunctionality: A Pressure-Induced Spin-Crossover Photomagnet. *J. Am. Chem. Soc.* **2015**, *137* (27), 8795-8802.
(55) Pittala, N.; Cuza, E.; Pinkowicz, D.; Magott, M.; Marchivie, M.; Boukheddaden, K.; Triki, S. Antagonist elastic interactions tuning spin crossover and LIESST behaviours in FeII trinuclear-based one-dimensional chains. *Inorg. Chem. Front.* **2022**, *9* (24), 6468-6481.
(56) Favre-Nicolin, V.; Cerny, R. FOX, `free objects for crystallography': a modular approach to ab initio structure determination from powder diffraction. *J. Appl. Crystallogr.* **2002**, *35* (6), 734-743.
(57) Petříček, V.; Dušek, M.; Palatinus, L. Crystallographic Computing System JANA2006: General features. *Z. Kristallogr. Cryst. Mater.* **2014**, *229* (5), 345-352.
(58) Steiner, T. The Hydrogen Bond in the Solid State. *Angew. Chem. Int. Ed.* **2002**, *41* (1), 48-76.
(59) Coronado, E.; Giménez-Marqués, M.; Mínguez Espallargas, G.; Rey, F.; Vitórica-Yrezábal, I. J. Spin-Crossover Modification through Selective CO2 Sorption. *J. Am. Chem. Soc.* **2013**, *135* (43), 15986-15989.
(60) Shin, J. W.; Jeong, A. R.; Jeoung, S.; Moon, H. R.; Komatsumaru, Y.; Hayami, S.; Moon, D.; Min, K. S. Three-dimensional iron(ii) porous coordination polymer exhibiting carbon dioxide-dependent spin crossover. *Chem. Commun.* **2018**, *54* (34), 4262-4265.
(61) Nakaya, M.; Kosaka, W.; Miyasaka, H.; Komatsumaru, Y.; Kawaguchi, S.; Sugimoto, K.; Zhang, Y.; Nakamura, M.; Lindoy, L. F.; Hayami, S. CO2-Induced Spin-State Switching at Room Temperature in a Monomeric Cobalt(II) Complex with the Porous Nature. *Angew. Chem. Int. Ed.* **2020**, *59* (26), 10658-10665.
(62) Decurtins, S.; Gütlich, P.; Köhler, C. P.; Spiering, H.; Hauser, A. Light-induced excited spin state trapping in a transition-metal complex: The hexa-1-propyltetrazole-iron (II) tetrafluoroborate spin-crossover system. *Chem. Phys. Lett.* **1984**, *105* (1), 1-4.
(63) Létard, J.-F. Photomagnetism of iron(ii) spin crossover complexes—the T(LIESST) approach. *J. Mater. Chem.* **2006**, *16* (26), 2550-2559.
(64) Chastanet, G.; Desplanches, C.; Baldé, C.; Rosa, P.; Marchivie, M.; Guionneau, P. *Chem. Sq.* **2018**, *2*, 2.
(65) Létard, J.-F.; Capes, L.; Chastanet, G.; Moliner, N.; Létard, S.; Real, J.-A.; Kahn, O. Critical temperature of the LIESST effect in iron(II) spin crossover compounds. *Chem. Phys. Lett.* **1999**, *313* (1), 115-120.
(66) Hauser, A. Reversibility of light-induced excited spin state trapping in the $Fe(ptz)_6(BF_4)_2$, and the $Zn_{1-x}Fe_x(ptz)_6(BF_4)_2$ spin-crossover systems. *Chem. Phys. Lett.* **1986**, *124* (6), 543-548.
(67) Matoga, D.; Szklarzewicz, J.; Mikuriya, M. $[PPh_4]_3[W(CN)_7(O_2)]\cdot 4H_2O$ as the Representative of the $[M(L)_7(LL)]$ Class for Nine-Coordinate Complexes. *Inorg. Chem.* **2006**, *45* (18), 7100-7104.
(68) Sheldrick, G. A short history of SHELX. *Acta Crystallogr. A* **2008**, *64* (1), 112-122.
(69) Sheldrick, G. Crystal structure refinement with SHELXL. *Acta Crystallogr. C* **2015**, *71* (1), 3-8.
(70) Dolomanov, O. V.; Bourhis, L. J.; Gildea, R. J.; Howard, J. A. K.; Puschmann, H. OLEX2: a complete structure solution, refinement and analysis program. *J. Appl. Crystallogr.* **2009**, *42* (2), 339-341.

Guest-Induced Pore Breathing Controls Spin State in a Cyanido-Bridged Framework

Michał Magott*,[ab‡] Klaudia Płonka,[a‡] Barbara Sieklucka,[a] Katarzyna Dziedzic-Kocurek,[c] Wataru Kosaka,[b] Hitoshi Miyasaka*,[b] Dawid Pinkowicz*,[a]

[a] Faculty of Chemistry, Jagiellonian University, Gronostajowa 2, 30-387 Kraków, Poland

[b] Institute for Materials Research, Tohoku University, 2-1-1 Katahira, Aoba-ku, Sendai 980-8577, Japan

[c] Marian Smoluchowski Institute of Physics, Jagiellonian University, Stanisława Łojasiewicza 11, Kraków 30-345, Poland

Table S1. Crystallographic data obtained from SCXRD for **1·4H₂O** and **1**.

	1·4H₂O (200 K)	**1** (200 K)	**1** (140 K)	**1** (80 K)
CCDC	2240344	2240345	2240346	2240347
Formula	$C_{56}H_{40}Fe_2N_{24}O_4W$	$C_{56}H_{32}Fe_2N_{24}W$		
FW / g mol^{-1}	1408.67	1336.60		
Crystal system	Tetragonal	Tetragonal		
Space group	$I4_1/a$	$I\bar{4}2d$ (refined as an inversion twin)		
a = b / Å	19.7947(3)	19.1966(4)	19.1481(4)	18.8695(4)
c / Å	16.0477(3)	15.8129(5)	15.7535(6)	15.4503(5)
V / Å^3	6288.0(2)	5827.2(3)	5776.0(3)	5501.2(3)
Z	4	4	4	4
ρ_{calc} / g cm^3	1.488	1.524	1.537	1.614
Abs. coeff. / mm^{-1}	2.34	2.52	2.54	2.67
F(000)	2808	2648		
Radiation source	Mo Kα	Mo Kα		
Crystal size / mm	0.24 x 0.10 x 0.08	0.12 x 0.11 x 0.06		
ϑ range / °	2.6-28.2	2.7-26.0	2.7-26.0	2.8-28.3
R_{int}	0.027	0.050	0.051	0.063
Parame-ters/restraints	204/3	193/3	193/0	193/0
GOF on F^2	1.10	1.14	1.16	1.11
R_1 (refl. with I > 2σ(I))	0.020	0.039	0.038	0.034
wR_2 (all reflections)	0.054	0.075	0.079	0.067
Largest diff. peak and hole / e Å^{-3}	0.75/-0.41	1.49/-2.49	1.34/-2.66	1.74/-2.46

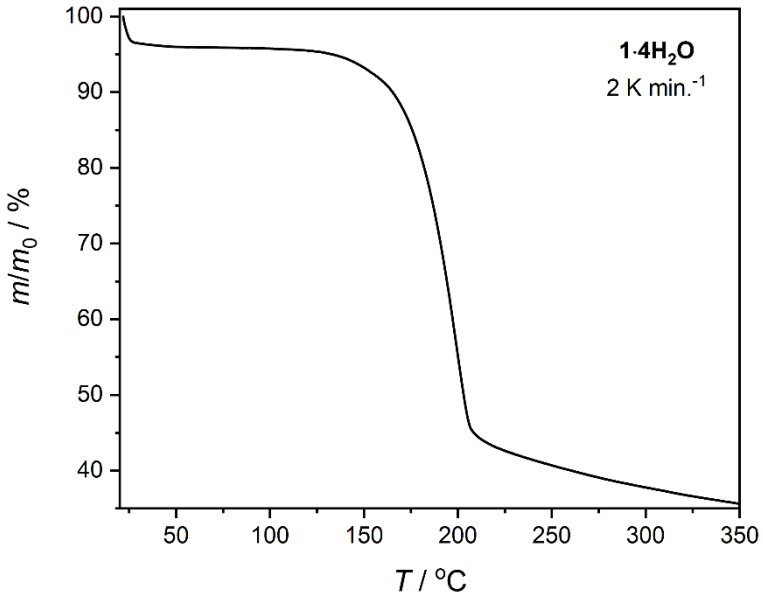

Figure S1. Thermogravimetric analysis of **1·4H₂O** recorded at a heating rate of 2 K min.$^{-1}$ under a dry nitrogen atmosphere.

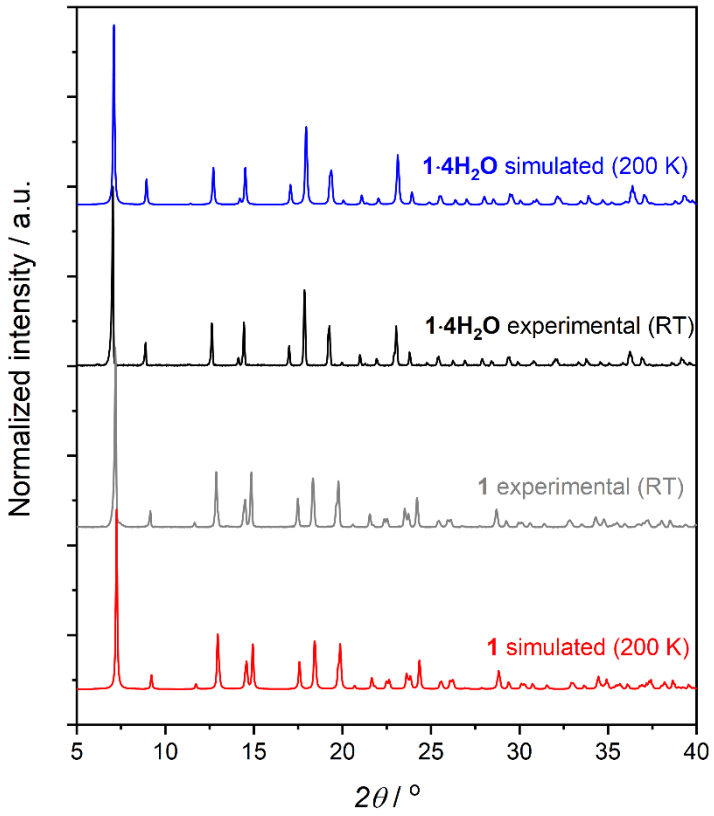

Figure S2. Powder X-ray diffraction pattern simulated from a single-crystal structure for **1·4H₂O** (blue line), experimental pattern for **1·4H₂O** (black line), experimental pattern for **1** (**1·4H₂O** activated at room temperature in vacuum – $p \approx 10^{-2}$ mbar; gray line) and simulated from a single-crystal structure for **1** (red line).

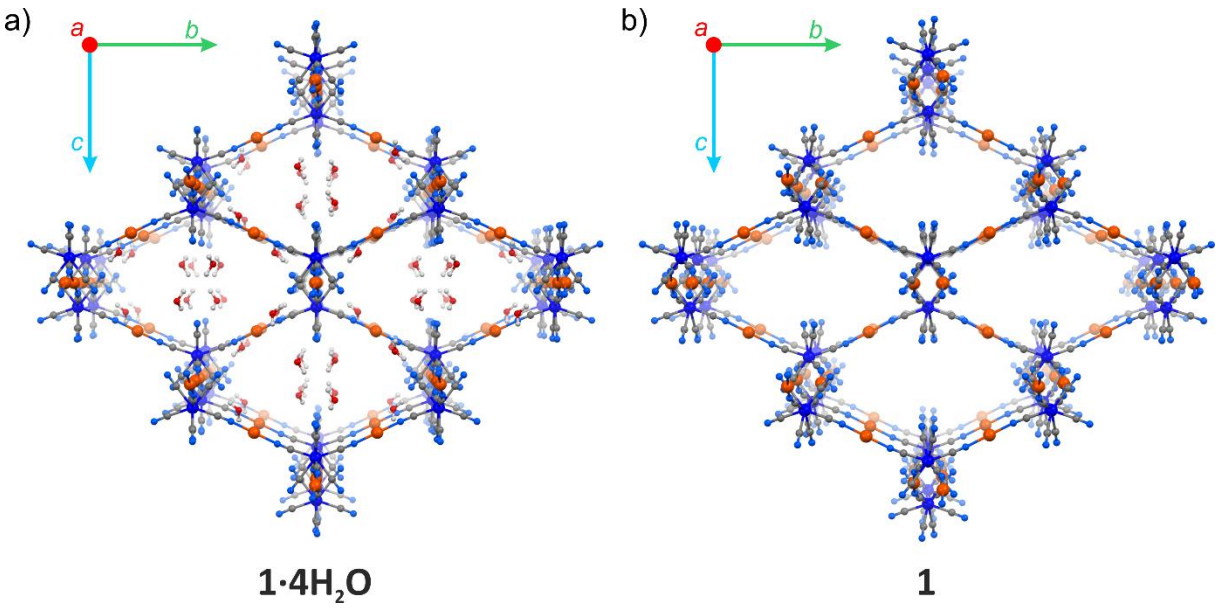

Figure S3. Crystal structures of **1·4H₂O** (a) and **1** (b) as seen along the crystallographic *a*-axis. 4-cyanopyridine molecules were omitted for clarity; W – dark blue, Fe – orange, O – red, N – blue, C – gray.

Table S2. Selected distances and bond length in structure of **1·4H₂O** and **1**.

		1·4H₂O (200 K)	**1** (200 K)	**1** (140 K)	**1** (80 K)
Bond lengths / Å	Fe-$N_{CN}1$	2.080(2)	2.085(7)	2.082(7)	1.958(5)
	Fe-$N_{py}3$	2.243(2)	2.207(13)	2.171(13)	2.016(9)
	Fe-$N_{py}5$	2.258(2)	2.252(7)	2.237(7)	2.070(6)
	Fe-$N_{py}7$	-	2.252(12)	2.251(13)	2.059(8)
Angles / °	$N_{CN}1$-Fe-$N_{CN}1$	180.0	175.8(4)	175.8(4)	174.2(3)
	$N_{CN}1$-Fe-$N_{py}3$	89.14(7)	87.9(2)	87.9(2)	87.1(2)
	$N_{CN}1$-Fe-$N_{py}5$	89.38(8)	89.3(2)	89.1(2)	89.7(2)
	$N_{CN}1$-Fe-$N_{py}7$	-	92.1(2)	92.1(2)	92.9(2)
	$N_{py}3$-Fe-$N_{py}5$	87.73(9)	90.0(2)	90.0(2)	90.6(1)
	$N_{py}3$-Fe-$N_{py}7$	-	180.0	180.0	180.0
	$N_{py}5$-Fe-$N_{py}5$	180.0	180.0(4)	179.9(4)	178.8(3)
	Fe-$N_{CN}1$-$C_{CN}1$	170.8(2)	162.4(7)	161.7(7)	165.2(5)
Intermolecular distances / Å	**hydrogen bond**				
	OH-N_{CN}	1.98(5)	-	-	-
	O-N_{CN}	2.867(4)	-	-	-
	OH-$N_{nitrile}$	2.30(5)	-	-	-
	O-$N_{nitrile}$	3.074(5)	-	-	-
	hydrogen bond				
	CH-N	2.695(4)	2.696(11)	2.661(10)	2.738(7)
	C-N	3.553(5)	3.43(2)	3.39(1)	3.44(1)
	nitrile-nitrile				
	N-C	3.244(6)	3.234(16)	3.224(12)	3.193(9)
		3.461(7)	3.362(10)	3.354(9)	3.296(6)

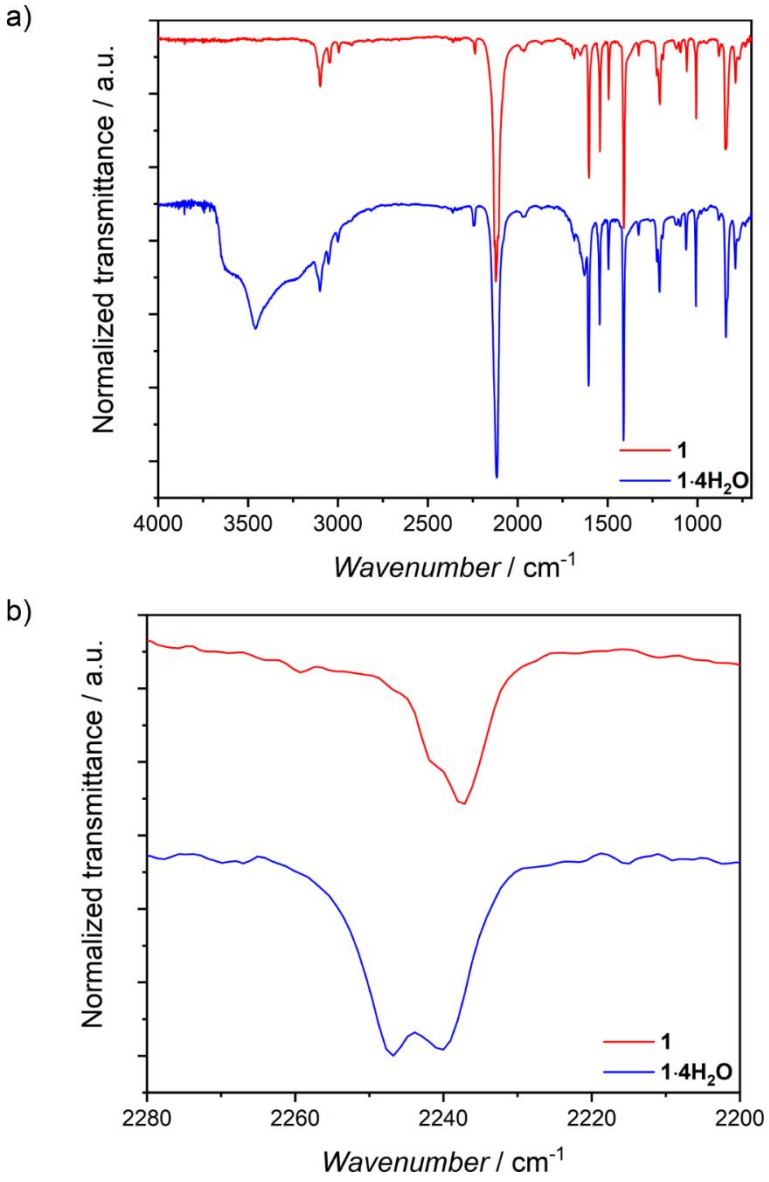

Figure S4. Infrared spectra of **1** and **1·4H₂O** recorded at room temperature using IR microscope in transmission mode (a) and close-up of the 2280-2000 cm^{-1} demonstrating the CN stretching band of 4-cyanopyridine ligands (b).

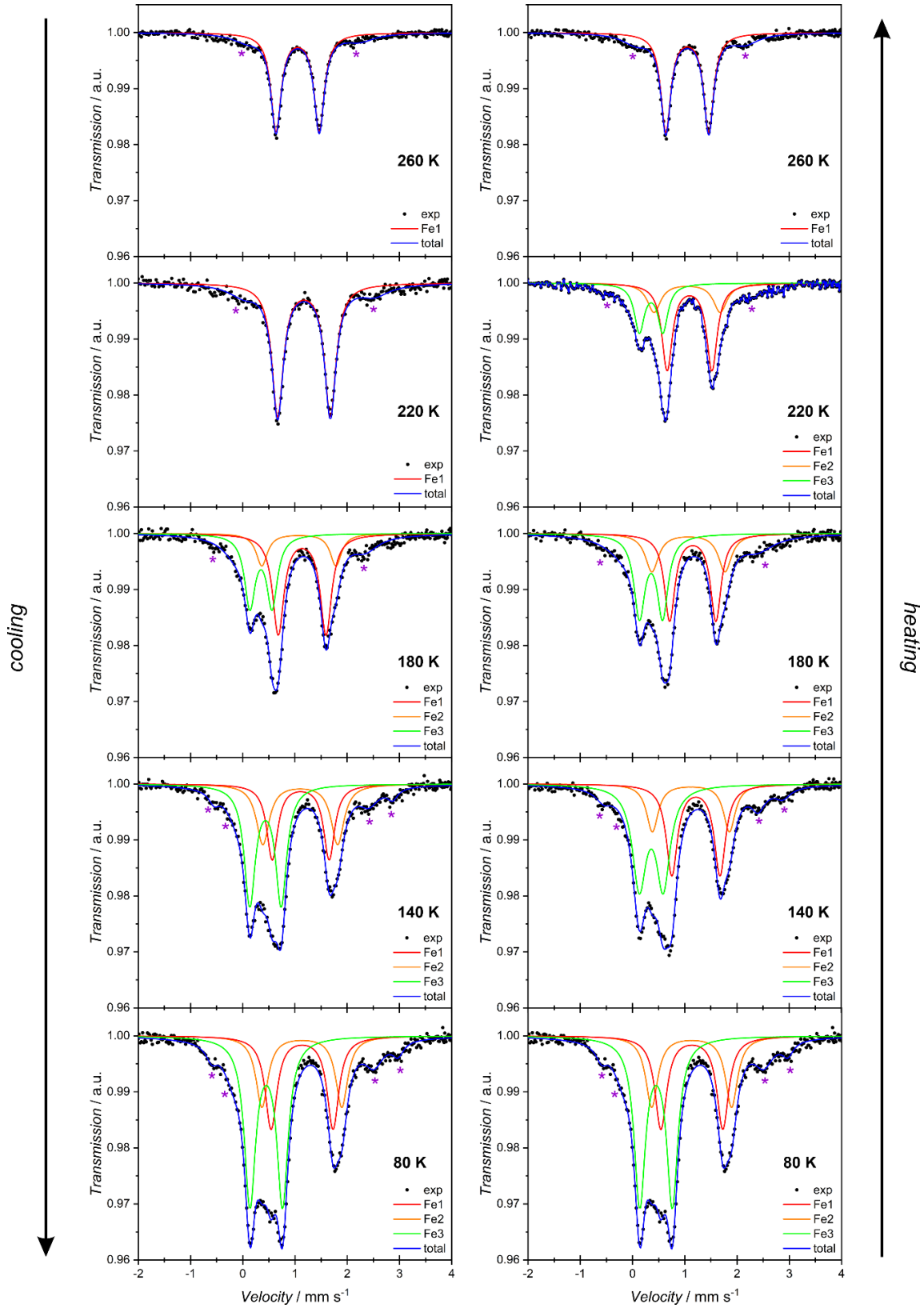

Figure S5. Sequence of experimental Mössbauer spectra obtained for **1·4H₂O** on cooling from 260 to 80 K and subsequent heating to 260 K (black points), and simulation (color lines). Purple asterisks denote small signals originating from the mother solution surrounding the solid. They were included in the fitting procedure, but the corresponding components were removed from Figure S5 for the sake of clarity.

Table S3. ^{57}Fe Mössbauer spectra parameters for **1·4H$_2$O**.

T **/ K**	**Fe site**	δ_{IS} **/ mm·s^{-1}**	ΔE_Q **/ mm·s^{-1}**	**fraction / %**
260(1) ↓	Fe1 (Fe^{II} HS)	1.05(1)	0.83(1)	100(1)
	Fe2 (Fe^{II} HS)	-	-	-
	Fe3 (Fe^{II} LS)	-	-	-
220(1) ↓	Fe1(Fe^{II} HS)	1.17(1)	1.01(1)	100(1)
	Fe2 (Fe^{II} HS)	-	-	-
	Fe3 (Fe^{II} LS)	-	-	-
180(1) ↓	Fe1 (Fe^{II} HS)	1.14(1)	0.91(1)	50(1)
	Fe2 (Fe^{II} HS)	1.08(1)	1.42(2)	16(1)
	Fe3 (Fe^{II} LS)	0.35(1)	0.42(1)	34(1)
140(1) ↓	Fe1 (Fe^{II} HS)	1.11(1)	1.09(1)	29(1)
	Fe2 (Fe^{II} HS)	1.10(1)	1.43(2)	26(1)
	Fe3 (Fe^{II} LS)	0.44(1)	0.60(1)	45(1)
80(1) ↓	Fe1 (Fe^{II} HS)	1.14(1)	1.19(1)	28(1)
	Fe2 (Fe^{II} HS)	1.13(1)	1.53(2)	23(1)
	Fe3 (Fe^{II} LS)	0.45(1)	0.62(1)	49(1)
140(1) ↑	Fe1 (Fe^{II} HS)	1.22(1)	0.92(1)	35(1)
	Fe2 (Fe^{II} HS)	1.12(1)	1.48(1)	19(1)
	Fe3 (Fe^{II} LS)	0.36(1)	0.46(3)	46(1)
180(1) ↑	Fe1 (Fe^{II} HS)	1.16(1)	0.89(1)	40(1)
	Fe2 (Fe^{II} HS)	1.07(1)	1.40(2)	22(1)
	Fe3 (Fe^{II} LS)	0.36(1)	0.44(1)	38(1)
220(1) ↑	Fe1 (Fe^{II} HS)	1.09(1)	0.86(1)	51(1)
	Fe2 (Fe^{II} HS)	1.05(1)	1.27(3)	22(1)
	Fe3 (Fe^{II} LS)	0.36(1)	0.45(1)	27(1)
260(1) ↑	Fe1 (Fe^{II} HS)	1.05(1)	0.82(1)	100(1)
	Fe2 (Fe^{II} HS)	-	-	-
	Fe3 (Fe^{II} LS)	-	-	-

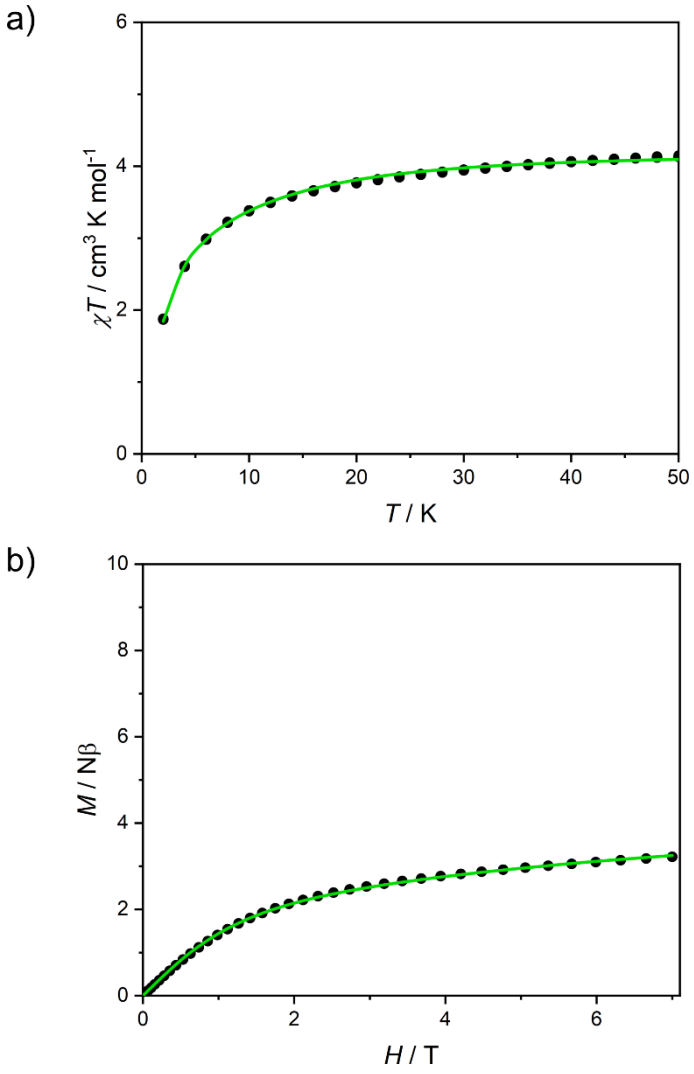

Figure S6. $\chi T(T)$ under $\mu_0 H_{dc}$ = 0.1 T (a) and $M(H)$ at T = 2.0 K (b) recorded for **1·4H₂O**. Green lines demonstrate the best fit to the equation 1 described in the text of the main article, which affords the following parameters: g_{eff}^2 = 7.61(1), D = 9.1(1) cm^{-1}, E = 2.5(1) cm^{-1} and zJ = -0.012(1) cm^{-1}.

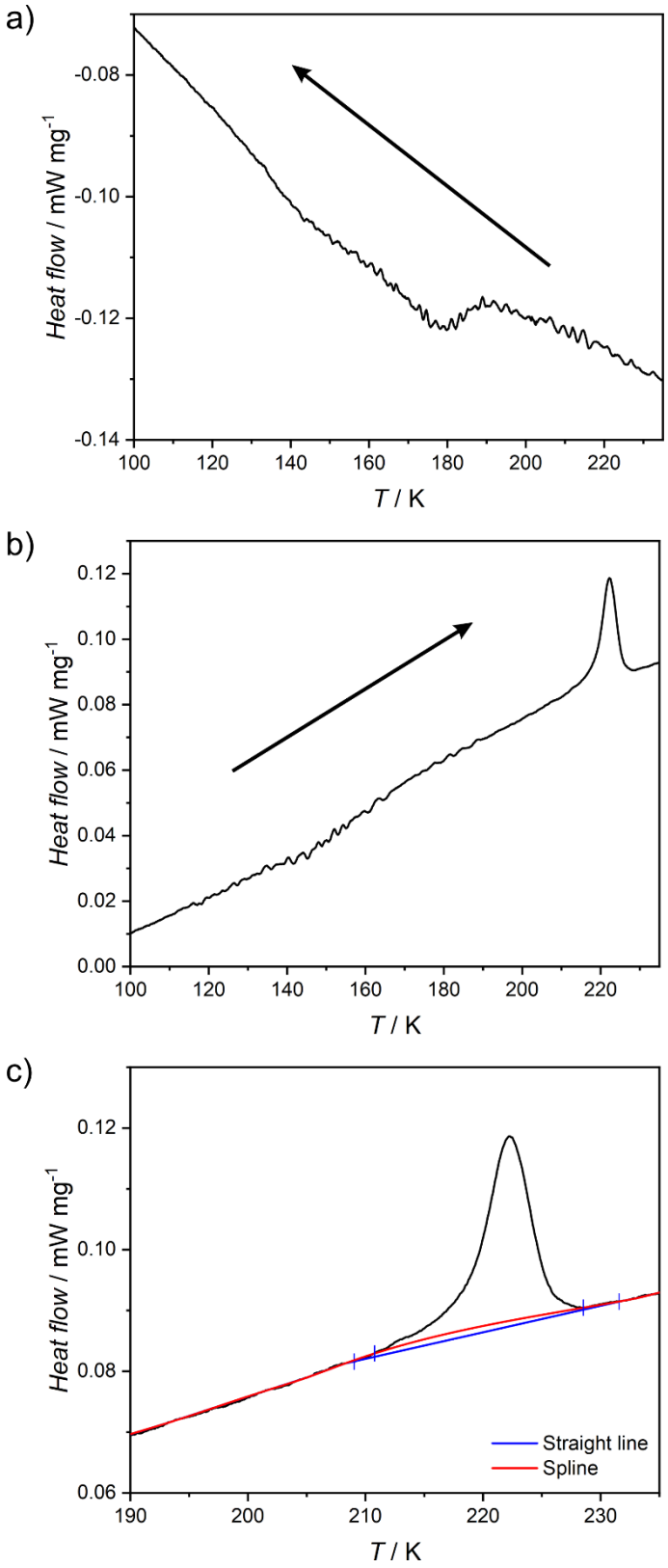

Figure S7. Dynamic scanning calorimetry (DSC) curves recorded at a scanning rate of 5 K min.$^{-1}$ on cooling (a) and heating (b) of **1·4H$_2$O**, as well as different types of background subtraction procedures used for determination of ΔH_{HL} value from the heating curve (c).

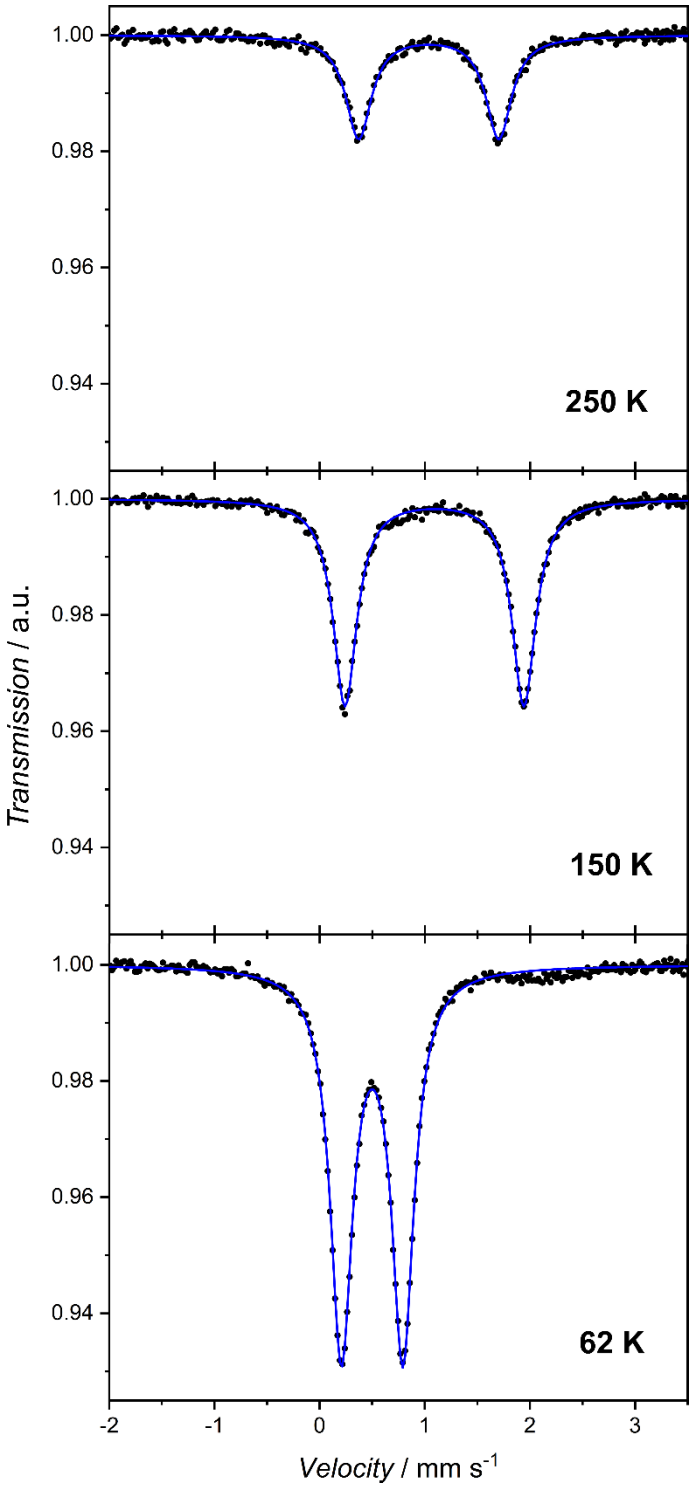

Figure S8. Mössbauer spectra obtained for **1** on cooling (black points) and single-component simulated signals (blue lines).

Table S4. ^{57Fe} Mössbauer spectra parameters for **1**.

T / K	Fe site	δ_{IS} / mm·s^{-1}	ΔE_Q / mm·s^{-1}	fraction / %
250(1) ↓	Fe (HS)	1.04(1)	1.33(1)	100 %
	Fe (LS)	-	-	-
150(1) ↓	Fe (HS)	1.05(1)	0.82(1)	100 %
	Fe (LS)	-	-	-
62(1) ↓	Fe (HS)	-	-	-
	Fe (LS)	0.50(1)	0.56(1)	100 %

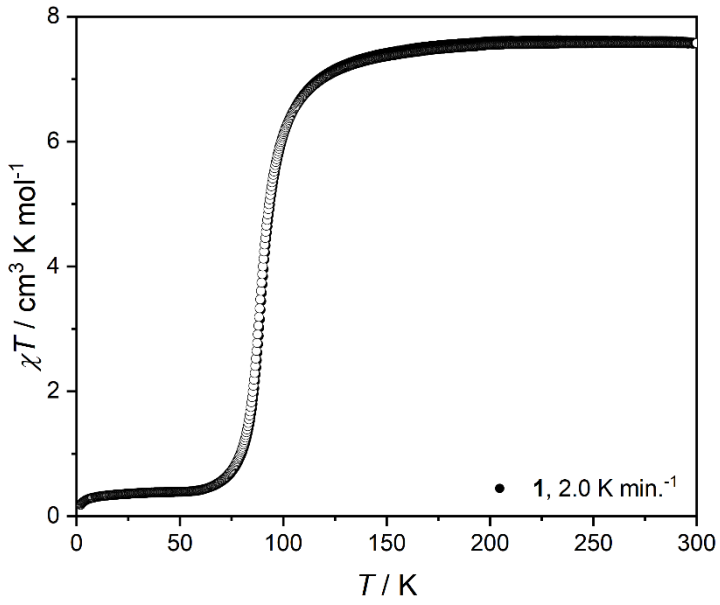

Figure S9. $\chi T(T)$ dependence recorded for **1** at 2 K min.$^{-1}$ on cooling (full circles) and heating (open circles) under $\mu_0 H_{dc}$ = 0.1 T.

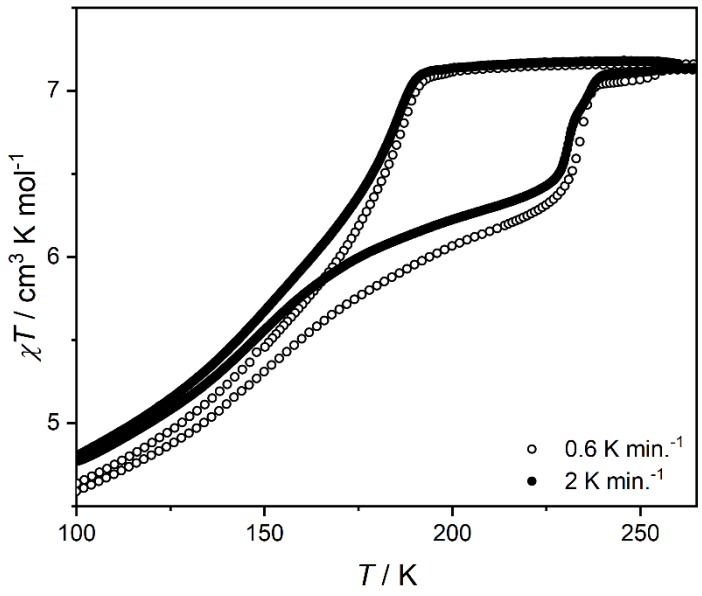

Figure S10. $\chi T(T)$ dependence recorded for **1·4H₂O** at 0.6 K min.$^{-1}$ with temperature stabilized at each point (open circles) and with constant 2 K min.$^{-1}$ sweep (black points) under $\mu_0 H_{dc} = 0.1$ T.

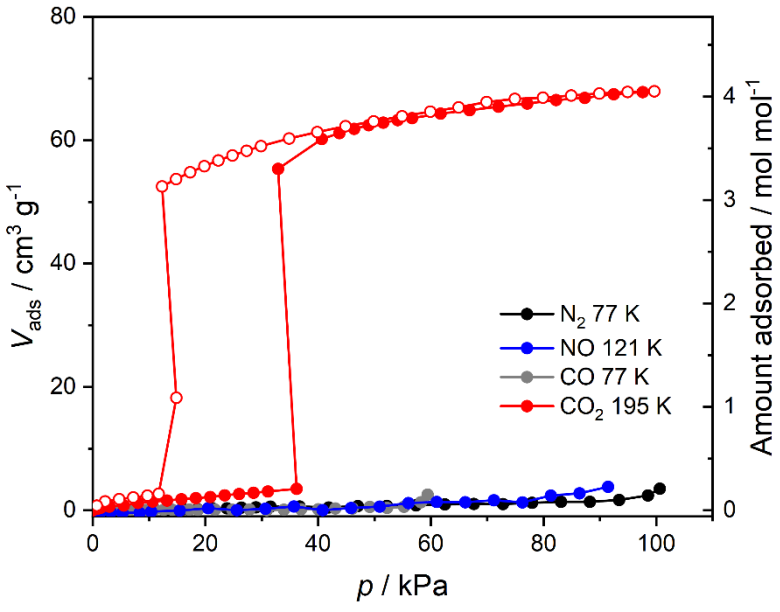

Figure S11. Volumetric measurement of gas adsorption for N_2, NO, CO and CO_2 in **1** (**1·4H₂O** activated at 323 K). Full circles – adsorption, open circles – desorption. Solid lines are guides for the eye.

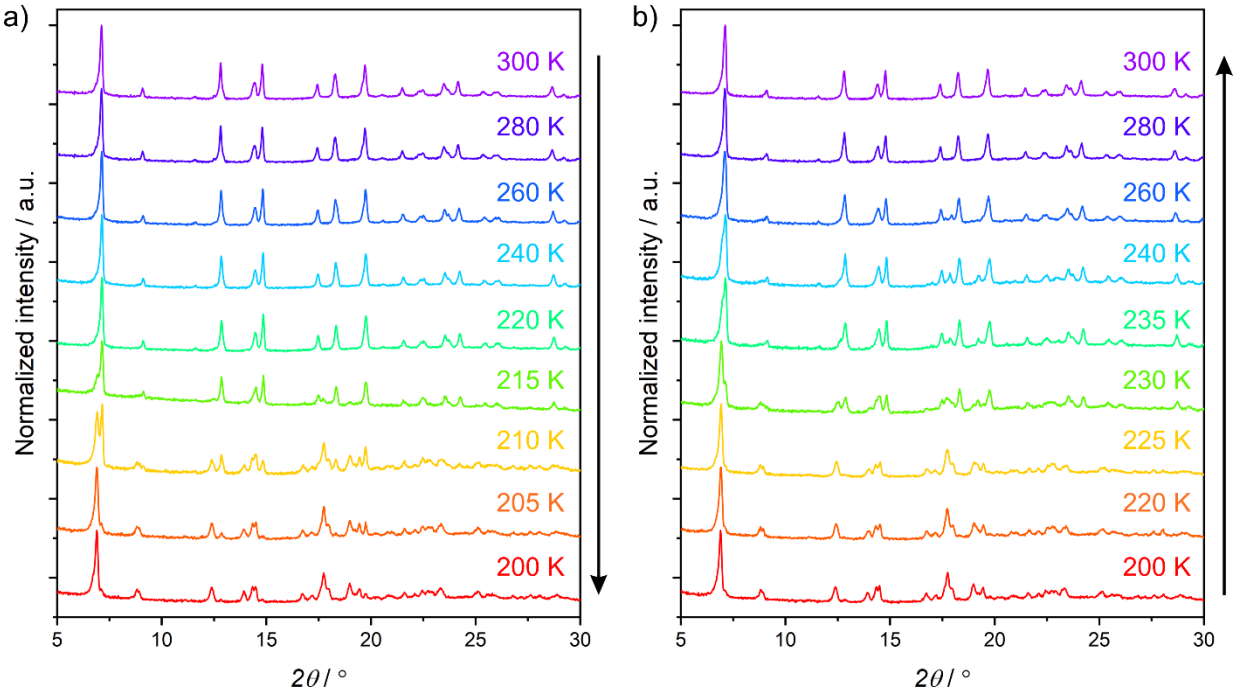

Figure S12. Powder X-ray diffraction patterns obtained for **1** under 100 kPa CO_2 atmosphere on cooling (a) and heating (b).

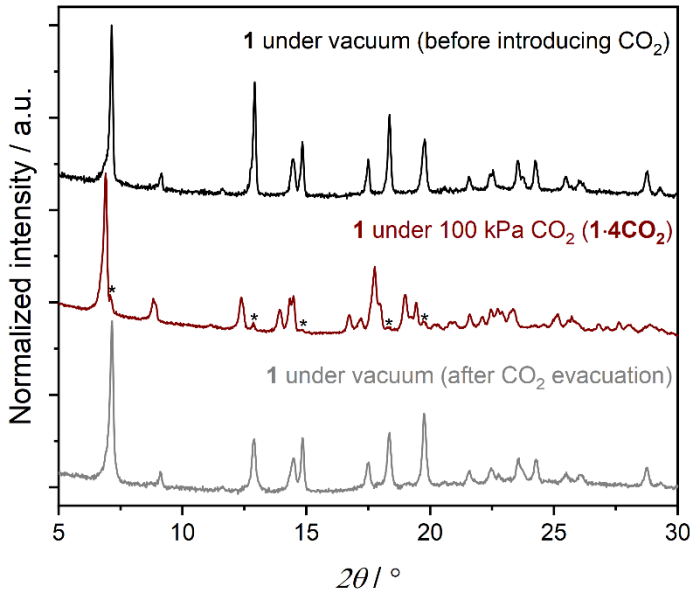

Figure S13. Powder X-ray diffraction patterns recorded for **1** at 200 K under vacuum (black line), under 100 kPa CO_2 atmosphere (dark red line), and after CO_2 removal (gray line). Asterisks denote the remnant reflections of phase **1** in **1·4CO₂**, which result from a small amount of powdered sample localized outside the cryocooler stream.

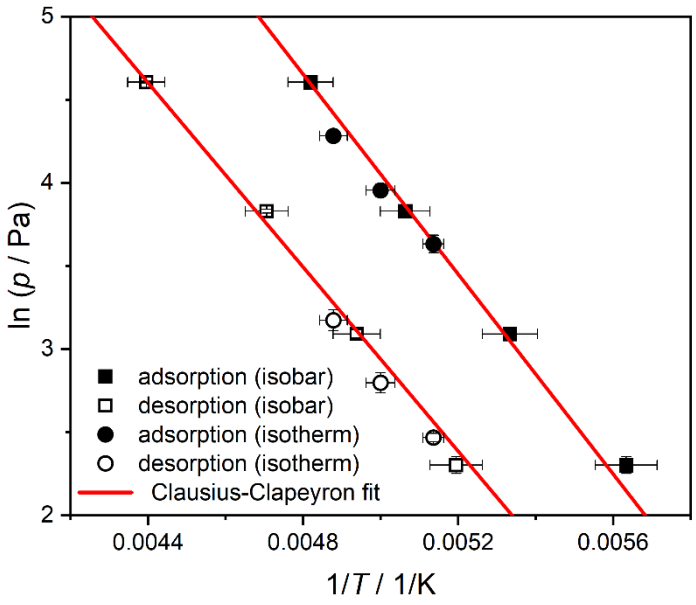

Figure S14. Clausius-Clapeyron fits of gate-opening (adsorption) and gate-closing (desorption) CO_2 pressure-temperature dependence for the transformation of **1** to **1·4CO₂** (and reverse).

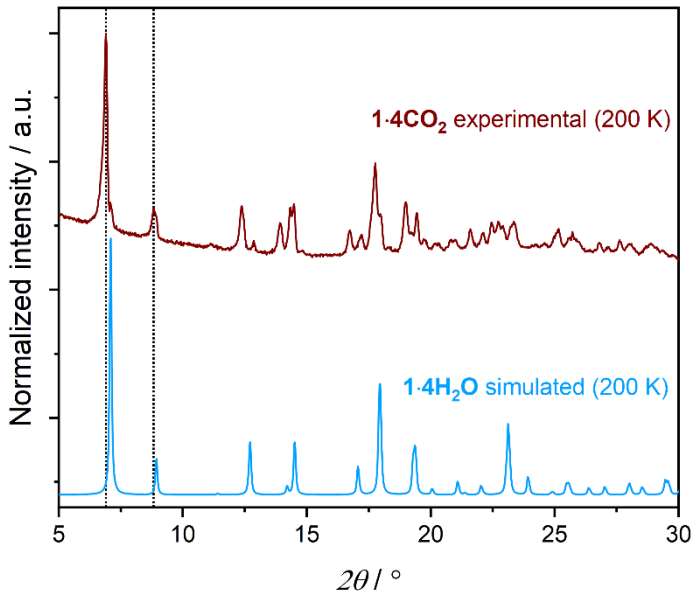

Figure S15. Comparison of the experimental PXRD pattern for **1·4CO₂** at 200 K (dark red line) and the simulated pattern for **1·4H₂O** at 200 K (blue line). The dotted lines show the shift in the position of the first two reflections, which in case of **1·4H₂O** correspond to the (101) and (200) Miller indices.

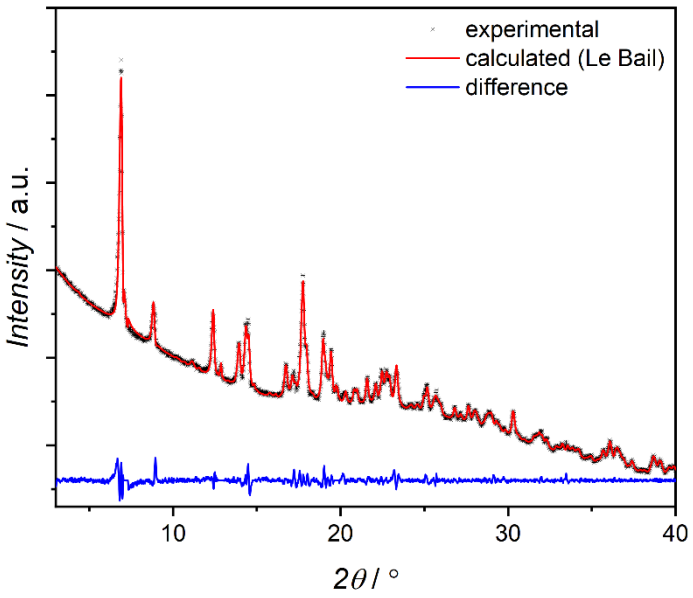

Figure S16. Comparison of the experimental PXRD pattern for **1·4CO₂** at 200 K (black points) and the Le Bail simulation for the orthorhombic unit cell (a = 20.364(3) Å, b = 19.950(3) Å, c = 16.461(3) Å and V = 6687(3) Å^3; red line), as well as the differential plot (I_c-I_o, blue line). The following regions containing reflections of phase **1** were excluded from simulation: [7.04, 7.30], [12.70, 13.00], [14.73,14.90] and [19.63,19.90].

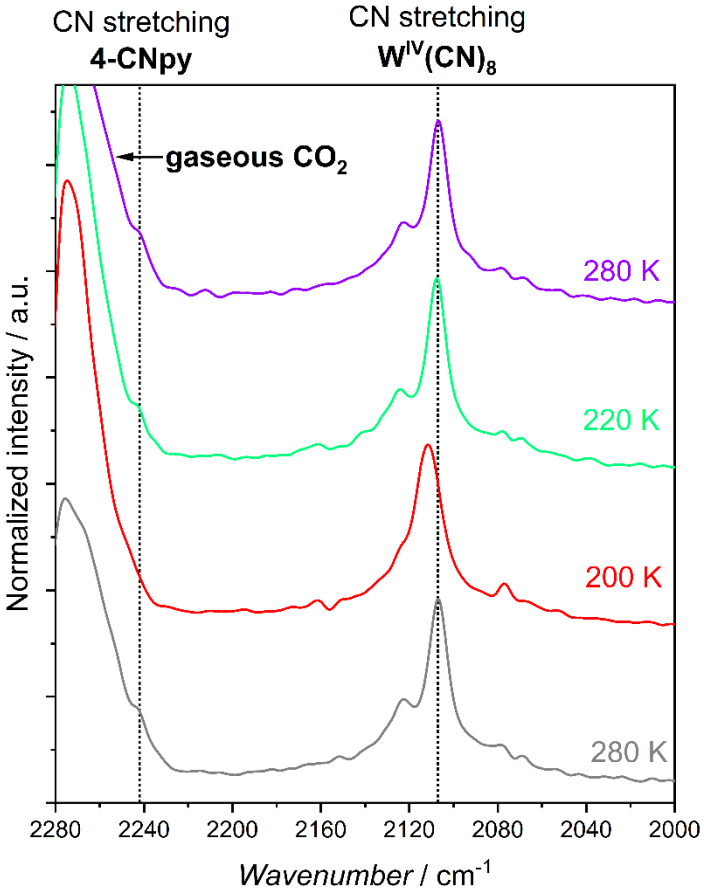

Figure S17. IR spectra recorded for **1** under 100 kPa CO_2 atmosphere at 280 K (purple line), 220 K (green line), 200 K (corresponding to the transition to **1·4CO₂**, red line) and after heating back to 280 K (which restores the initial **1**, gray line).

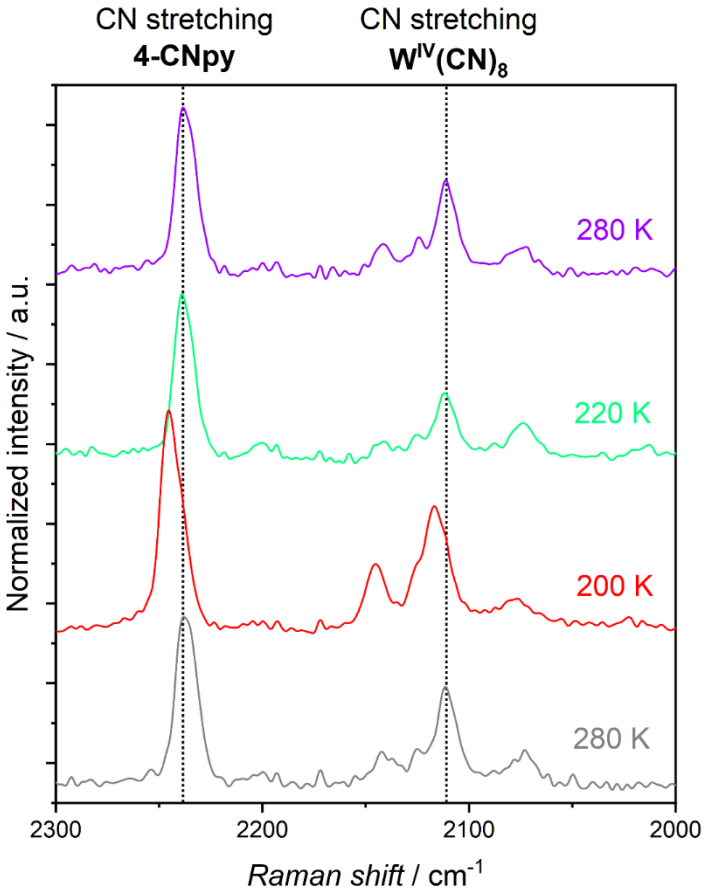

Figure S18. Raman spectra recorded for **1** under 100 kPa CO_2 atmosphere at 280 K (purple line), 220 K (green line), 200 K (corresponding to the transition to **1·4CO₂**, red line) and after heating back to 280 K (which restores the initial **1**, gray line).

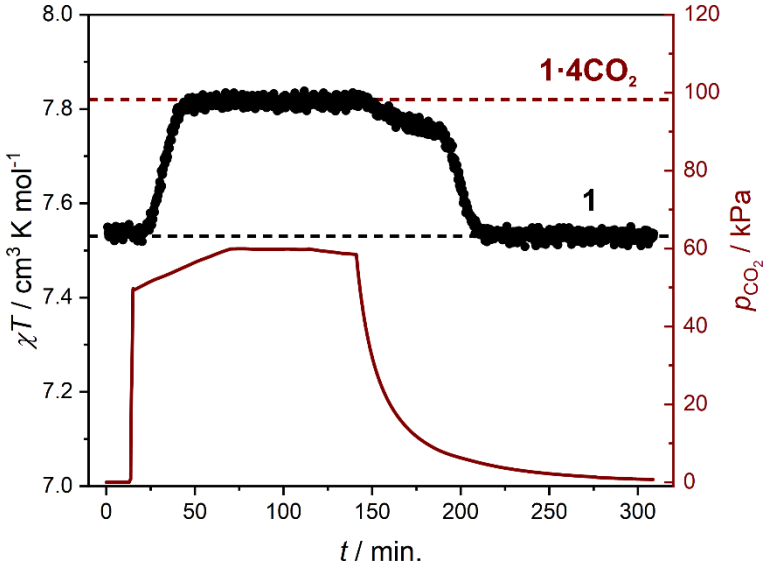

Figure S19. Time dependence of χT at $\mu_0 H_{dc}$ = 0.1 T (black line) and CO_2 pressure in the system (dark red line) during isothermal *in situ* CO_2 sorption experiment performed for **1** at 195 K.

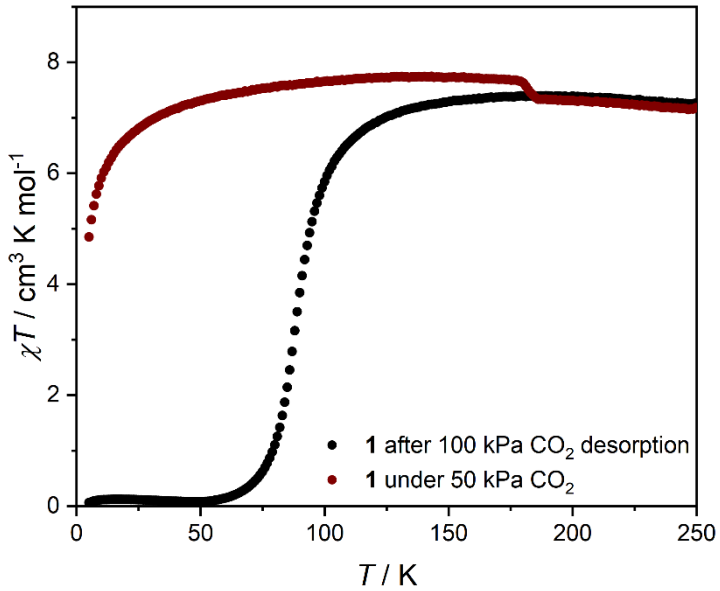

Figure S20. $\chi T(T)$ at $\mu_0 H_{dc}$ = 0.1 T recorded for **1** under 100 kPa He atmosphere (black line), after the *in situ* 100 kPa CO_2 adsorption experiment shown in the Figure 6, and the following measurement under 50 kPa CO_2 + 5 kPa He atmosphere (dark red line).

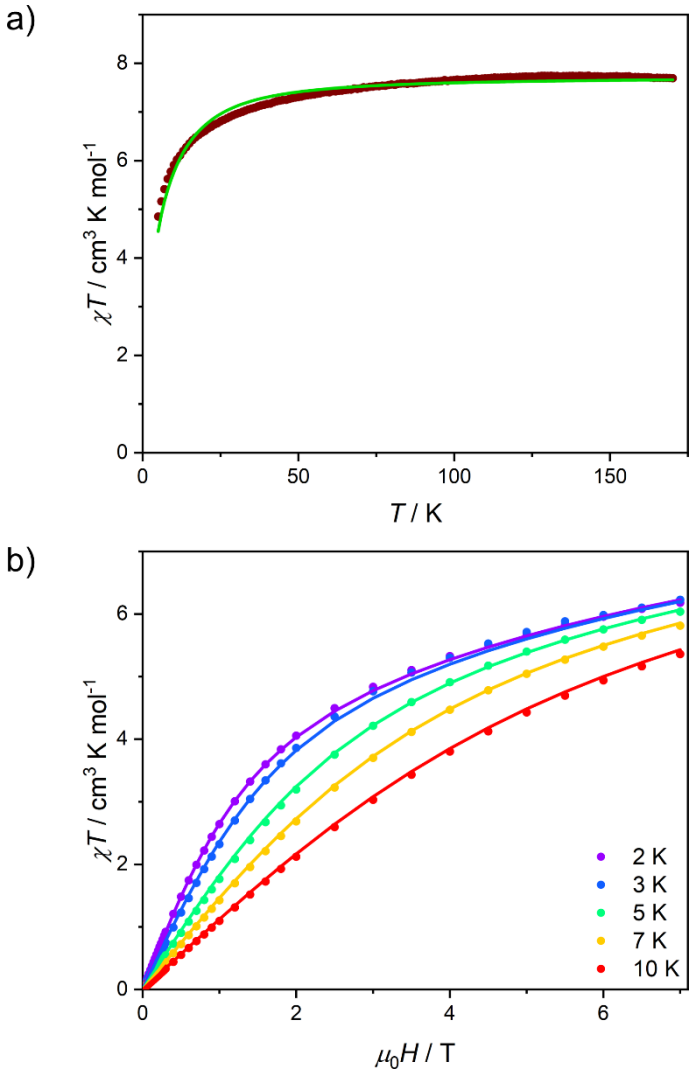

Figure S21. $\chi T(T)$ under $\mu_0 H_{dc}$ = 0.1 T (a) and $M(H)$ at T = 2-10 K (b) recorded for **1·4CO₂** (**1** under 50 kPa CO_2 atmosphere). Solid lines demonstrate the best fit to the equation 1 described in the main article text, which gives the following parameters: g = 2.27(5), D = 9.0(1) cm^{-1}, E = 2.3(1) cm^{-1} and zJ = -0.085(1) cm^{-1}.

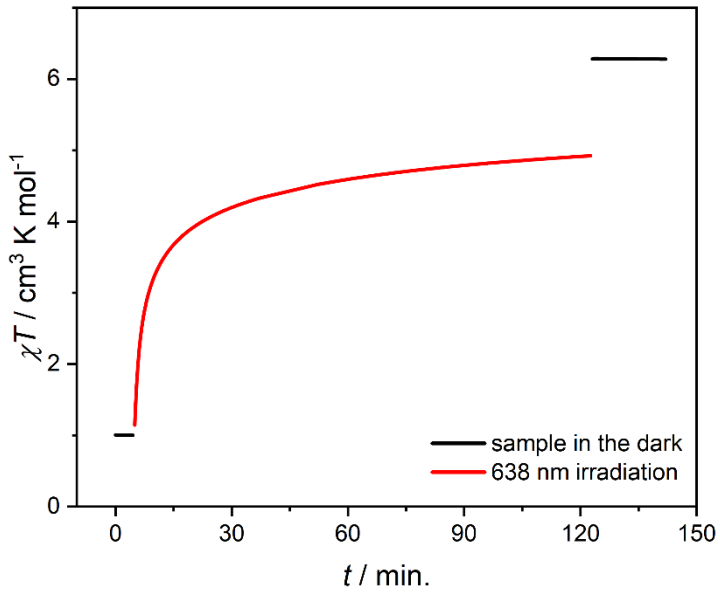

Figure S22. $\chi T(t)$ dependence recorded for **1** at $\mu_0 H_{dc}$ = 0.1 T during the 638 nm irradiation experiment.

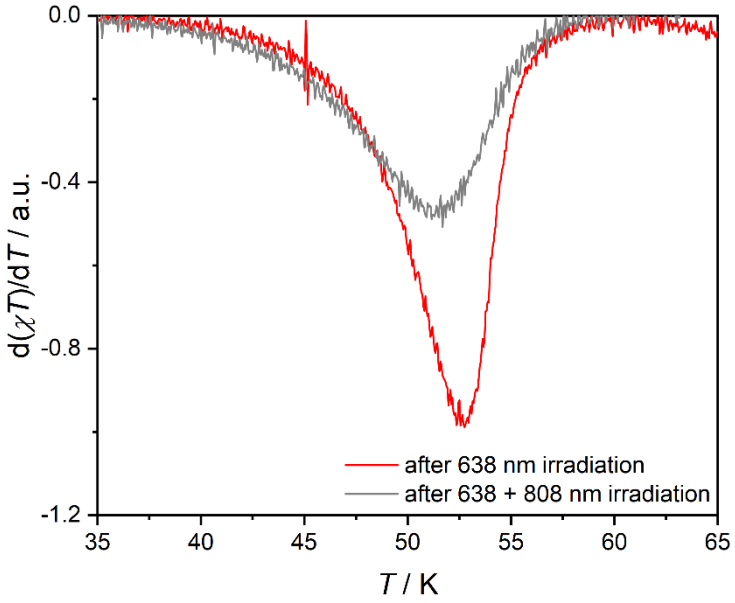

Figure S23. Derivative of $\chi T(T)$ curves for **1** after light irradiation (depicted in the Figure 4a).

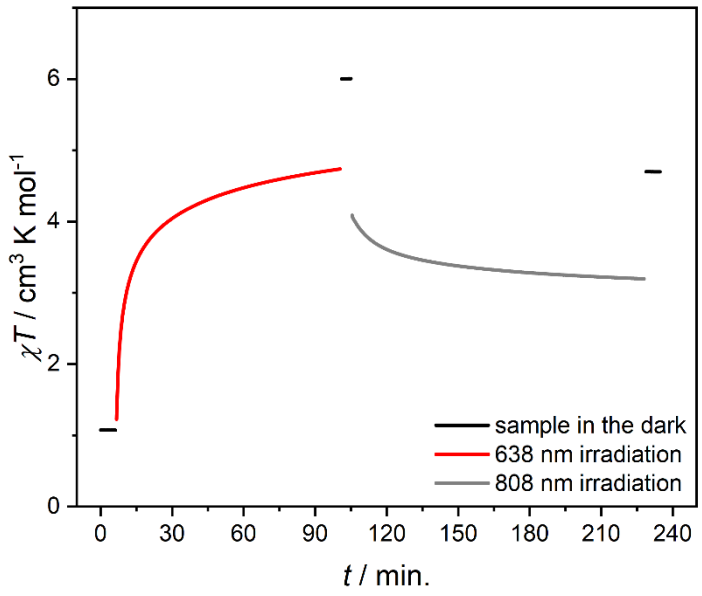

Figure S24. $\chi T(t)$ dependence recorded for **1** at $\mu_0 H_{dc}$ = 0.1 T during the 638 and 808 nm irradiation experiment.

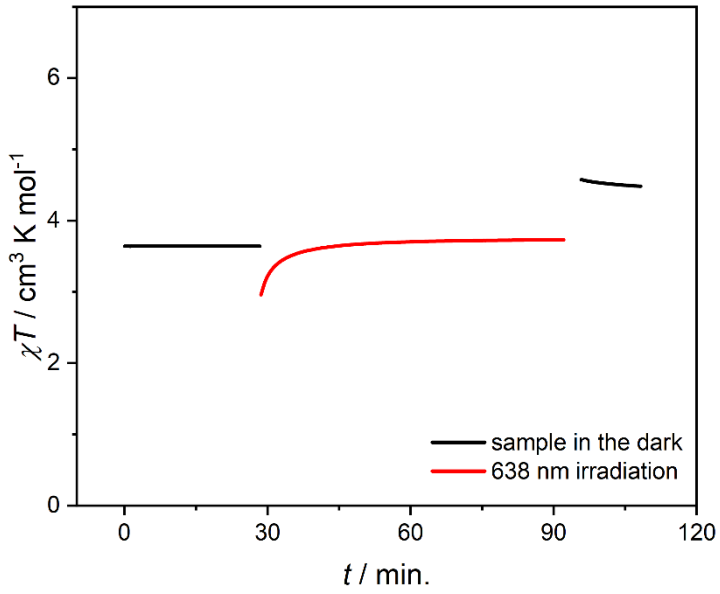

Figure S25. $\chi T(t)$ dependence recorded for **1·4H₂O** at $\mu_0 H_{dc}$ = 0.1 T during the 638 nm irradiation experiment.

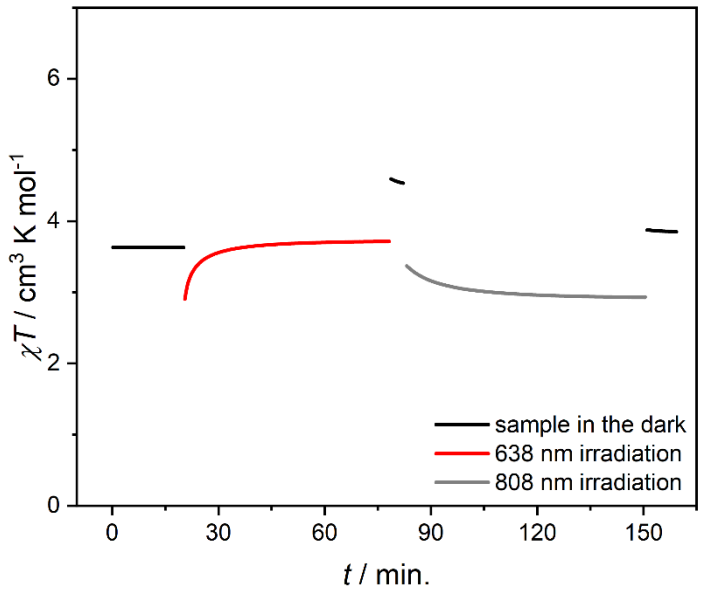

Figure S26. $\chi T(t)$ dependence recorded for **1·4H₂O** at $\mu_0 H_{dc}$ = 0.1 T during the 638 and 808 nm irradiation experiment.

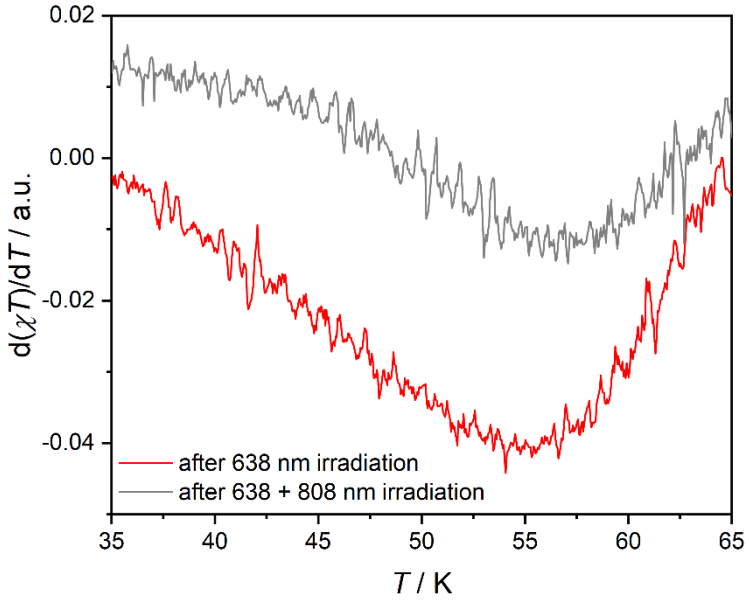

Figure S27. Derivative of $\chi T(T)$ curves for **1·4H₂O** after light irradiation (depicted in the Figure 4b).

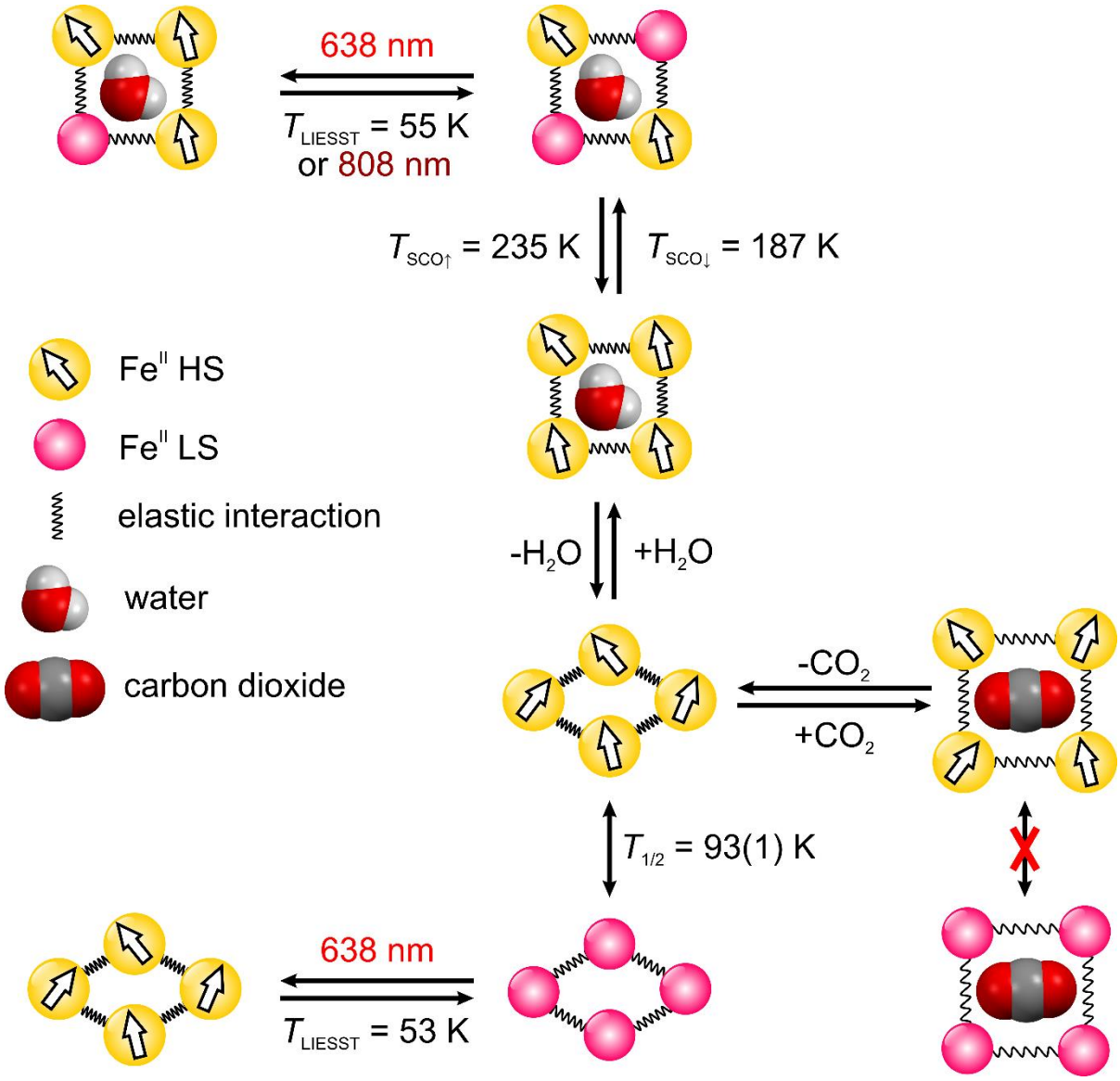

Figure S28. Schematic depiction of temperature-, light- and sorption-induced changes in the spin state of **1.**